Extended High-Frame Rate Imaging Method with Limited-Diffraction Beams

Jiqi Cheng and Jian-yu Lu, *Senior Member, IEEE*

***Abstract*—Fast three-dimensional (3-D) ultrasound imaging is a technical challenge. Previously, a high-frame rate (HFR) imaging theory was developed in which a pulsed plane wave was used in transmission, and limited-diffraction array beam weightings were applied to received echo signals to produce a spatial Fourier transform of object function for 3-D image reconstruction. In this paper, the theory is extended to include explicitly various transmission schemes such as multiple limited-diffraction array beams and steered plane waves. A relationship between the limited-diffraction array beam weighting of received echo signals and a 2-D Fourier transform of the same signals over a transducer aperture is established. To verify the extended theory, computer simulations, *in vitro* experiments on phantoms, and *in vivo* experiments on the human kidney and heart were performed. Results show that image resolution and contrast are increased over a large field of view as more and more limited-diffraction array beams with different parameters or plane waves steered at different angles are used in transmissions. Thus, the method provides a continuous compromise between image quality and image frame rate that is inversely proportional to the number of transmissions used to obtain a single frame of image. From both simulations and experiments, the extended theory holds a great promise for future HFR 3-D imaging.**

I. Introduction

A single-frequency beam with a Bessel transverse profile was developed by Stratton and termed "undistorted progressive wave" [1]. Forty-six years later, Durnin [2] and Durnin *et al.* [3] studied the Bessel beam again and termed the beam "nondiffracting beam" or "diffraction-free beam". Because Durnin's terminologies are controversial in the scientific community and practical beams will eventually diffract, we termed the propagation-invariant beams or waves "limited diffraction beams" [4]. The advantage of limited diffraction beams is that, even if they are produced with finite aperture and energy, they have a very large depth of field. Because of this property, limited diffraction beams and other related beams are extensively studied by many researchers [5]–[48]. One class of limited diffraction beams is called X wave [44], [45] and has been investigated by many physicists [49]–[56]. Recently, X waves have been applied to nonlinear optics; and, due to their importance, they were reported in the "Search and Discovery" column of [57].

From limited diffraction beam studies, a high-frame rate imaging theory was developed in 1997 [27], [28] in which a pulsed plane wave was used in transmission, and limited-diffraction array beam weightings were applied to received echo signals to produce a spatial Fourier transform of object function for 3-D image reconstruction. Because one transmission can be used to reconstruct an image, high image frame rate can be achieved. In addition, because Fourier transform can be implemented with a fast Fourier transform (FFT) that is computationally efficient, simpler imaging systems could be constructed to implement the method. High-frame rate imaging is important for imaging of fast moving objects such as the heart, especially, in 3-D imaging in which many 2-D image frames are needed to form a 3-D volume that may reduce image frame rate dramatically with conventional imaging methods. Because of the importance of the high-frame rate imaging method, it was noted as one of the predictions of the 21st century medical ultrasonics [58]. Furthermore, the use of steered plane waves in transmissions to increase image field of view and reduce speckle noises [27], [28], [59], [60] or the use of limited-diffraction array beams in transmission to increase field of view and spatial Fourier domain coverage to increase image resolution [26]–[28] was suggested. Images reconstructed with different steering angles can be combined with a coherent (enhancing resolution) or incoherent superposition (reducing speckles) [27], [28]. To increase field of view, a method using a spherical wave transmission followed by Fourier transformation for image reconstruction also has been proposed [14]. Although the method may maintain a high-frame rate at a large field of view due to the divergence nature of spherical waves, it may lower signal-to-noise ratio (SNR) and reduce computation efficiency as compared to the high-frame rate imaging method.

In this paper, the theory of high-frame rate imaging [27], [28] is extended to include explicitly various transmission schemes such as multiple limited-diffraction array beams and steered plane waves [61], [62] (the first report was given in [61]). The extended theory includes the earlier suggestions of using these transmission schemes [26]–[28]. In addition, limited-diffraction array beam weightings of received echo signals over a 2-D transducer aperture are proved to be the same as a 2-D Fourier transform of these signals over the same aperture [61], [62]. To verify the extended theory, computer simulations, *in vitro* experiments on phantoms, and *in vivo* experiments on the human kid-

Manuscript received July 8, 2005; accepted October 22, 2005. This work was supported in part by the grant, HL60301, from the National Institute of Health, USA.

The authors are with the Ultrasound Laboratory, Department of Bioengineering, The University of Toledo, Toledo, OH 43606 (e-mail: jilu@eng.utoledo.edu).

ney and heart are performed. Results show that image resolution and contrast are increased over a large field of view as more and more limited-diffraction array beams with different parameters or plane waves steered at different angles are transmitted. Thus, the method provides a continuous compromise between image quality and image frame rate that is inversely proportional to the number of transmissions used in a single frame of image. This is useful because in some applications, such as imaging of liver and kidney in which high-frame rate imaging is not crucial, high quality images can be obtained at the expense of image-frame rate.

It is worth noting that there are advantages [62] for using limited-diffraction array beam transmissions [26]–[28] as compared to using multiple plane waves steered at different angles. Limited-diffraction array beam transmissions can be produced with an amplitude weighting of transducer aperture (no need of any time or phase delay) [62]. This potentially allows a single or a few transmitters to excite transducer elements of different weighting amplitudes at the same time and greatly simplifying imaging systems, especially in 3-D imaging in which over 10,000 independent, linear high-voltage, high-power transmitters otherwise may be required in some applications [62]. Because all elements of the transducer are excited at the same time for limited diffraction beams, dead zones due to strong ringing or interelement interferences of transmission pulses are reduced. In addition, a limited-diffraction array beam weighting acts as a diffraction grating in which a lower frequency component is steered at a larger angle than a higher frequency one. This may help to increase image field of view with a broadband transducer though it may be at the expenses of reduced energy density that may lower SNR. The other advantage is that limited-diffraction array beam in transmission could be used to obtain the transverse component of flow velocity [29], [37]. The disadvantage may be that, due to aperture weighting, the total transmission energy may be reduced by half in addition to the diffraction grating effects in some cases.

The theory of high-frame rate imaging and its extension have connections to many previous studies in which Fourier transform also was used for ultrasonic imaging in the past two decades. However, the previous studies are not aimed at increasing the frame rate of conventional B-mode images. For example, Norton and Linzer [63] and Nagai [64], [65] have developed a Fourier-domain reconstruction method for synthetic focusing by solving the inverse scattering problem. A point source was used to transmit a broadband spherical wave over any given geometrical surfaces. The 2-D or 3-D images are reconstructed using Fourier transformation. Apparently, the imaging process is slow. Soumekh [66] has developed a Fourier-based method using a fixed focus transmission and reception (cofocal) approach. This method requires multiple transmissions to cover the Fourier space of object function and thus is slow. Another method of Soumekh [67] used a plane wave steered at different angles to form a line of data in the Fourier space. Unfortunately, this method also requires a large number of transmissions to reconstruct a frame of image. Ylitalo and Ermert [68] and Ylitalo [69] suggested a narrow-band imaging method based on ultrasound holography and synthetic aperture concept. Busse [70] also applied synthetic aperture focusing with Fourier transform to get C-mode images (the image plane is in parallel with the surface of a planar transducer). The drawbacks of synthetic aperture methods are that they suffer from low transmission efficiency because only part of the aperture of a transducer is used. Because a large amount of transmissions are required to reconstruct an image, the image-frame rate is low in addition to poor quality due to a low SNR. Nonetheless, Fourier-based synthetic aperture imaging is used with catheter-based ultrasound probes when a complex method is difficult to implement due to the confined space of these probes [71]–[73]. Benenson *et al.* [74] have suggested a Fourier-based 3-D imaging method with mechanically scanning of a highly focused, single-element transducer. Although the method may get a high-resolution image beyond the focal distance and may have applications in ophthalmology and dermatology, it is not suitable for high-frame rate imaging because mechanical scanning is usually very slow. Jeong *et al.* [75], [76] also suggested an imaging method that could be used to improve image resolution and contrast by transmitting multiple plane waves to coherently synthesize the so-called sinc waves. However, their method uses a time-domain approach and the complexity of an imaging system would be formidably high if it is applied to 3-D imaging at a rate of a few thousands volumes/second.

This paper is organized as follows. In Section II, the theory extended from (15) of [27] will be presented [61], [62]. The proof that limited-diffraction array beam weightings of received echo signals over a 2-D transducer aperture are the same as a 2-D Fourier transform of these signals over the same aperture also will be presented [61], [62]. Results of some previous studies will be given as special cases of the extended theory. The mapping between the Fourier domains of echo signals and object function will be introduced in Section III, followed by Section IV for computer simulations, and Section V for *in vitro* experiments on phantoms and *in vivo* experiments of the human kidney and heart using the high-frame rate imaging system [62], [77], [78]. Discussion and conclusions will be given in Sections VI and VII, respectively.

II. Theory

In this section, the theory of high-frame rate imaging [27], [28] is extended to include explicitly various transmission schemes such as multiple limited-diffraction array beams and steered plane waves (the derivations will be in parallel with those in [27]) [61], [62]. The proof that limited-diffraction array beam weightings of received echo signals over a 2-D transducer aperture are the same as a 2-D Fourier transform of these signals over the same aperture is also given [61], [62].

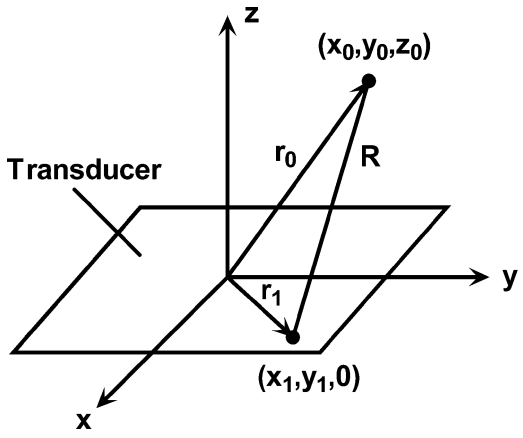

Fig. 1. Coordinates of transducer and object in space.

A. Extension of High-Frame Rate Imaging Theory

As shown in Fig. 1, a 2-D array transducer located at $z = 0$ plane is excited to generate a broadband, limited-diffraction array beam or a steered pulsed plane wave. The same transducer also is used to receive echoes scattered from objects. The aperture of the transducer is assumed to be infinitely large, and the size of each transducer element is infinitely small. The coordinates on the surface of the transducer are denoted as $\vec{r}_1 = (x_1, y_1, 0)$, and the coordinates of any spatial point in the object are given by $\vec{r}_0 = (x_0, y_0, z_0)$. In the following, (15) of [27] will be generalized to include explicitly various transmission schemes such as multiple limited-diffraction array beams and steered plane waves.

Assuming that the transmitting transfer function of the transducer is $A(k)$ that includes both electrical response of the driving circuits and electro-acoustical coupling characteristics [79] of the transducer elements. Then, a broadband, limited-diffraction array beam [29], [32] or pulsed steered plane wave (a plane wave is a special case of limited diffraction beams) incident on the object can be expressed as [see (5) and (6) of [27] and their derivations from X waves [44], [45]]:

$$\Phi^T_{\text{Array}}(\vec{r}_0, t) = \frac{1}{2\pi}\int_0^\infty A(k)e^{ik_{x_T}x_0+ik_{y_T}y_0+ik_{z_T}z_0}e^{-i\omega t}dk$$
$$= \frac{1}{2\pi}\int_{-\infty}^\infty A(k)H(k)e^{ik_{x_T}x_0+ik_{y_T}y_0+ik_{z_T}z_0}e^{-i\omega t}dk, \quad (1)$$

where the superscript "T" in $\Phi^T_{\text{Array}}(\vec{r}_0, t)$ means transmission and the subscript Array represents array beam, and

$$\tilde{\Phi}^T_{\text{Array}}(\vec{r}_0, \omega) = \frac{A(k)H(k)}{c}e^{ik_{x_T}x_0+ik_{y_T}y_0+ik_{z_T}z_0}, \quad (2)$$

is the Fourier transform (spectrum) of the array beams in terms of time. Eq. (2) is an expression of a monochromatic (single angular frequency ω) plane wave steered at a direction along the transmission wave vector, $\vec{K}^T = (k_{x_T}, k_{y_T}, k_{z_T})$.

$$H\left(\frac{\omega}{c}\right) = \begin{cases} 1, & \omega \geq 0 \\ 0, & \omega < 0 \end{cases}, \quad (3)$$

is the Heaviside step function [80], and

$$k_{z_T} = \sqrt{k^2 - k_{x_T}^2 - k_{y_T}^2} \geq 0, \quad (4)$$

where k_{x_T} and k_{y_T} are projections of the transmission wave vector along x_1 and y_1 axes, respectively, $k = \omega/c$ is the wave number, where $\omega = 2\pi f$ is the angular frequency, f is the temporal frequency, c is the speed of sound of the object, and t is the time.

Due to the reciprocal principle, the response of a transducer weighted with a broadband limited diffraction array beam [29], [32] or pulsed steered plane wave for a point source (or scatterer) located at $\vec{r}_0 = (x_0, y_0, z_0)$ is given by:

$$\Phi^R_{\text{Array}}(\vec{r}_0, t) = \frac{1}{2\pi}\int_{-\infty}^\infty T(k)H(k)e^{ik_x x_0+ik_y y_0+ik_z z_0}e^{-i\omega t}dk$$
$$\text{or} \quad (5)$$
$$\tilde{\Phi}^R_{\text{Array}}(\vec{r}_0, \omega) = \frac{T(k)H(k)}{c}e^{ik_x x_0+ik_y y_0+ik_z z_0},$$

where the superscript "R" in $\Phi^R_{\text{Array}}(\vec{r}_0, t)$ means reception, $\tilde{\Phi}^R_{\text{Array}}(\vec{r}_0, \omega)$ is the Fourier transform (spectrum) of $\Phi^R_{\text{Array}}(\vec{r}_0, t)$ in terms of time, which is an expression of a monochromatic plane wave response steered at a direction along the reception wave vector $\vec{K}^R = (k_x, k_y, k_z)$ [similar to (2) above], $T(k)$ is the transfer function of the transducer in reception, and:

$$k_z = \sqrt{k^2 - k_x^2 - k_y^2} \geq 0, \quad (6)$$

where k_x and k_y are projections of the reception wave vector along x_1 and y_1 axes, respectively.

If the same array transducer is used as both transmitter and receiver above, from (1) and (5), the received signal for the wave scattered from a point scatterer located at $\vec{r}_0 = (x_0, y_0, z_0)$ is given by the following convolution [(12) of [27]]:

$$R^{(\text{one})}_{k_x+k_{x_T},k_y+k_{y_T},k_z+k_{z_T}}(t) =$$
$$f(\vec{r}_0)\left[\Phi^T_{\text{Array}}(\vec{r}_0, t)^* \Phi^R_{\text{Array}}(\vec{r}_0, t)\right]$$
$$= \frac{1}{2\pi}\int_{-\infty}^\infty \frac{A(k)T(k)H(k)}{c}$$
$$\times f(\vec{r}_0)e^{i(k_x+k_{x_T})x_0+i(k_y+k_{y_T})y_0+i(k_z+k_{z_T})z_0}e^{-i\omega t}dk, \quad (7)$$

where "$*$" represents the convolution with respect to time and where the superscript "one" means one point scatterer. This uses the fact that the spectrum of the convolution of two functions is equal to the product of the spectra

of the functions. And $f(\vec{r}_0)$ is an object function that is related to the scattering strength of a scatterer at point $\vec{r}_0$.

Assuming that the imaging system is linear and multiple scattering can be ignored (Born or weak scattering approximation [81], [82]), the received signal for echoes returned from all random scatterers within the object $f(\vec{r}_0)$ is a linear superposition of those echo signals from individual point scatterers as follows (see (13) of [27]):

$$\begin{aligned} R_{k_x+k_{x_T},k_y+k_{y_T},k_z+k_{z_T}}(t) &= \frac{1}{2\pi}\int_{-\infty}^{\infty}\frac{A(k)T(k)H(k)}{c} \\ &\times\left[\int_V f(\vec{r}_0)e^{i(k_x+k_{x_T})x_0+i(k_y+k_{y_T})y_0+i(k_z+k_{z_T})z_0}d\vec{r}_0\right]e^{-i\omega t}dk \\ &= \frac{1}{2\pi}\int_{-\infty}^{\infty}\frac{A(k)T(k)H(k)}{c}F\left(k_x+k_{x_T},k_y+k_{y_T},k_z+k_{z_T}\right) \\ &\times e^{-i\omega t}dk. \quad (8) \end{aligned}$$

The 3-D Fourier transform pair in this expression is defined as follows:

$$\begin{aligned} F(k_x,k_y,k_z) &= \int_V f(\vec{r}_0)e^{ik_xx_0+ik_yy_0+ik_zz_0}d\vec{r}_0 \\ &\text{and} \\ f(\vec{r}_0) &= \frac{1}{(2\pi)^3}\int_{-\infty}^{\infty}\int_{-\infty}^{\infty}\int_{-\infty}^{\infty}F(k_x,k_y,k_z) \quad (9) \\ &\times e^{-ik_xx_0-ik_yy_0-ik_zz_0}dk_xdk_ydk_z, \end{aligned}$$

where V is the volume of the object $f(\vec{r}_0)$.

From (8) the temporal Fourier transform (spectrum) of the received signal can be obtained (see (15) of [27], which establishes a relationship between the Fourier transform of the object function and the Fourier transform of the received echo signals) [61], [62]:

$$\begin{aligned} \tilde{R}_{k_x+k_{x_T},k_y+k_{y_T},k_z+k_{z_T}}(\omega) &= \frac{A(k)T(k)H(k)}{c^2} \\ &\times\int_V f(\vec{r}_0)e^{i\left(k_x+k_{x_T}\right)x_0+i\left(k_y+k_{y_T}\right)y_0+i\left(k_z+k_{z_T}\right)z_0}d\vec{r}_0 \end{aligned}$$

or

$$\begin{aligned} \tilde{R}_{k_x+k_{x_T},k_y+k_{y_T},k_z+k_{z_T}}(\omega) &= \frac{A(k)T(k)H(k)}{c^2} \quad (10) \\ &\times F\left(k_x+k_{x_T},k_y+k_{y_T},k_z+k_{z_T}\right) \end{aligned}$$

or

$$F_{BL}(k'_x,k'_y,k'_z) = c^2H(k)\tilde{R}_{k'_x,k'_y,k'_z}(\omega),$$

where:

$$\begin{cases} k'_x = k_x+k_{x_T} \\ k'_y = k_y+k_{y_T} \\ k'_z = k_z+k_{z_T} = \sqrt{k^2-k_x^2-k_y^2}+\sqrt{k^2-k_{x_T}^2-k_{y_T}^2} \geq 0 \end{cases} \quad (11)$$

The $H(k)$ in (10) is used to indicate that only positive values of k are used and thus it can be applied to either side of the equation (for the convenience of presentation), it is used with $\tilde{R}_{k'_x,k'_y,k'_z}(\omega)$, and (see (16) of [27]).

$$F_{BL}(k'_x,k'_y,k'_z) = A(k)T(k)F(k'_x,k'_y,k'_z) \quad (12)$$

is a band-limited version of the spatial Fourier transform of the object function, the subscript BL means band-limited.

It should be emphasized that (10) is also a 2-D Fourier transform of the echo signals in terms of both x_1 and y_1 over the transducer surface (aperture) [61], [62]. The proof is given as follows. Using (5), one can easily see that (10) can be rewritten as:

$$\begin{aligned} \tilde{R}_{k_x+k_{x_T},k_y+k_{y_T},k_z+k_{z_T}}(\omega) &= \frac{A(k)T(k)H(k)}{c^2} \\ &\times\int_V f(\vec{r}_0)e^{ik_xx_0+ik_yy_0+ik_zz_0}e^{ik_{x_T}x_0+ik_{y_T}y_0+ik_{z_T}z_0}d\vec{r}_0 \\ &= \frac{A(k)}{c}\int_V f(\vec{r}_0)\left[\frac{T(k)H(k)}{c}e^{ik_xx_0+ik_yy_0+ik_zz_0}\right] \\ &\times e^{ik_{x_T}x_0+ik_{y_T}y_0+ik_{x_T}z_0}d\vec{r}_0 \\ &= \frac{A(k)}{c}\int_V f(\vec{r}_0)\left[\tilde{\Phi}^R_{\text{Array}}(\vec{r}_0,\omega)\right]e^{ik_{x_T}x_0+ik_{y_T}y_0+ik_{z_T}z_0}d\vec{r}_0 \\ &= \frac{A(k)}{c}\int_V f(\vec{r}_0)\left[\Im_{x_1,y_1}\left\{\tilde{E}(x_1,y_1;\vec{r}_0;\omega)\right\}\right] \quad (13) \\ &\times e^{ik_{x_T}x_0+ik_{y_T}y_0+ik_{z_T}z_0}d\vec{r}_0 \\ &= \Im_{x_1,y_1}\left\{\int_V\left[f(\vec{r}_0)\frac{A(k)}{c}e^{ik_{x_T}x_0+ik_{y_T}y_0+ik_{z_T}z_0}\right]\right. \\ &\left.\times\tilde{E}(x_1,y_1;\vec{r}_0;\omega)d\vec{r}_0\right\}, \end{aligned}$$

where $\Im_{x_1,y_1}$ represents a 2-D Fourier transform in terms of both x_1 and y_1 at the transducer surface,

$$\begin{aligned} \tilde{E}(x_1,y_1;\vec{r}_0;\omega) &= \Im^{-1}_{k_x,k_y}\left\{\tilde{\Phi}^R_{\text{Array}}(\vec{r}_0,\omega)\right\} \\ &= \frac{T(k)H(k)}{c}\Im^{-1}_{k_x,k_y}\left\{e^{ik_xx_0+ik_yy_0+ik_zz_0}\right\} \\ &= -\frac{T(k)H(k)}{2\pi c}\frac{\partial}{\partial z_0} \quad (14) \\ &\times\left(\frac{e^{ik\sqrt{(x_1-x_0)^2+(y_1-y_0)^2+z_0^2}}}{\sqrt{(x_1-x_0)^2+(y_1-y_0)^2+z_0^2}}\right), \end{aligned}$$

where $\Im^{-1}_{k_x,k_y}$ represents an inverse 2-D Fourier transform in terms of both k_x and k_y. The last equal sign in (14) is obtained with the shift theorem of Fourier transform, and the following Fourier transformation equality (see (13) of [83]):

$$\begin{aligned} e^{ik_xx_0+ik_yy_0+ik_zz_0} &= -\frac{1}{2\pi}\Im_{x_1,y_1} \\ &\times\left\{\frac{\partial}{\partial z_0}\left(\frac{e^{ik\sqrt{(x_1-x_0)^2+(y_1-y_0)^2+z_0^2}}}{\sqrt{(x_1-x_0)^2+(y_1-y_0)^2+z_0^2}}\right)\right\}. \quad (15) \end{aligned}$$

Apparently, $\tilde{E}(x_1,y_1;\vec{r}_0;\omega)$ in (14) is a differentiation of the Green's function [84] representing the field at a

point of the transducer surface, $(x_1, y_1, 0)$, produced by a point source (scatterer) located at a spatial point, $\vec{r}_0 = (x_0, y_0, z_0)$. This is also clear from the Rayleigh-Sommerfeld diffraction formula [(3-36) of [84], and [83]]:

$$\tilde{\Phi}(\vec{r}_0;\omega) = -\frac{1}{2\pi}\iint_{\sum_1} \tilde{\Phi}(\vec{r}_1;\omega)\frac{\partial}{\partial z_0} \times \left(\frac{e^{ik\sqrt{(x_1-x_0)^2+(y_1-y_0)^2+z_0^2}}}{\sqrt{(x_1-x_0)^2+(y_1-y_0)^2+z_0^2}}\right) d\vec{r}_1, \quad (16)$$

where $\sum_1$ is the area of the transducer surface, $\tilde{\Phi}(\vec{r}_0;\omega)$ is the integrated field distribution or response of the transducer for a point source (scatterer) at $\vec{r}_0$, and $\tilde{\Phi}(\vec{r}_1;\omega)$ is the weighting function at the surface of the transducer. It is seen that the kernel of (16) is the same as that of $\tilde{E}(x_1, y_1; \vec{r}_0; \omega)$ in (14). Therefore, (13) indicates that (10) represents a 2-D Fourier transform over the transducer surface for echo signals produced from all point scatterers in the volume, V. The phase and amplitude of each point source (scatterer) are modified by the transmitted plane wave, $(A(k)H(k)/c)e^{ik_{x_T}x_0+ik_{y_T}y_0+ik_{x_T}z_0}$ [see (2)] as well as the object function, $f(\vec{r}_0)$. Thus, limited-diffraction array beam weighting theory [27] is exactly the same as a 3-D Fourier transformation of echo signals over both the transducer aperture (2-D) and time (1-D), which decomposes echo signals into plane waves or limited diffraction array beams [29], [32]. The previous work [27], [28], [59], [60] on the steered plane waves and the limited-diffraction array beam weightings in transmissions is equivalent to the phase and amplitude modifications of the object function shown in (13) or (10). It is worth noting that, because both the high-frame rate imaging method [27] and current extension are based on the rigorous theory of the Green's function in (14) and (16), it could be more accurate to reflect the scatterer distributions in space than the simple delay-and-sum [85] method used in almost all commercial ultrasound scanners. This proves that $\tilde{R}_{k_x+k_{x_T},k_y+k_{y_T},k_z+k_{z_T}}(\omega)$ in (10) or (13) can be obtained directly by 3-D Fourier transform of the received echo signals over a 2-D transducer aperture and 1-D time!

Taking the inverse Fourier transformation of (12), an approximation of the object function can be reconstructed using the definition of the spatial Fourier transform in (9) (see (18) of [27]):

$$f(\vec{r}_0) \approx f_{BL}(\vec{r}_0) \approx f_{BL}^{\text{Part}}(\vec{r}_0) = \frac{1}{(2\pi)^3}\int_{-\infty}^{\infty}dk_x'\int_{-\infty}^{\infty}dk_y'\int_{k\geq\sqrt{k_{x_T}^2+k_{y_T}^2}\text{ and }k\geq\sqrt{k_x^2+k_y^2}}dk_z' \times F_{BL}(k_x', k_y', k_z')e^{-ik_x'x_0-ik_y'y_0-ik_x'z_0}, \quad (17)$$

where the first approximation is due to the finite bandwidth of received signals and the second one is due to the requirements that both $k \geq \sqrt{k_{x_T}^2 + k_{y_T}^2}$ and $k \geq \sqrt{k_x^2 + k_y^2}$ must be satisfied. Thus, only part (indicated by the superscript Part) of the spatial Fourier transform of the object function is known. It can be shown from computer simulations and experiments in the later sections that these approximations do not affect the quality of reconstructed images as compared to those obtained with conventional, dynamically focused pulse-echo imaging systems.

If the object function, $f(\vec{r}_0)$, is real, which is the case in most applications, the following is true from (9) (see (22) of [27]):

$$F(-k_x', -k_y', -k_z') = F^*(k_x', k_y', k_z'), \quad (18)$$

where the superscript "$*$" means complex conjugate. In this case, the spatial Fourier transform of the object function in the lower Fourier space ($k_z' < 0$) is also known.

In the following sections, (10), (11), and (17) will be used to reconstruct images for various transmission schemes.

B. Special Cases of the High-Frame Rate Imaging Theory

1. High-Frame Rate Imaging Method without Steering: For a plane wave without steering, one has $k_{x_T} = 0$ and $k_{y_T} = 0$. From (10) and (11), one obtains:

$$F_{BL}(k_x, k_y, k_z') = c^2H(k)\tilde{R}_{k_x,k_y,k_z'}(\omega), \quad (19)$$

where:

$$\begin{cases} k_x' = k_x \\ k_y' = k_y \\ k_z' = k + k_z = k + \sqrt{k^2 - k_x^2 - k_y^2} \geq 0 \end{cases}, \quad (20)$$

which is exactly the same as that of the high-frame rate imaging method (see (8) and (15) of [27]). From (19) and (20), 3-D or 2-D images can be reconstructed with (17) [27], [28].

2. Two-Way Dynamic Focusing with Limited Diffraction Array Beams: If both $k_x = k_{x_T}$ and $k_y = k_{y_T}$ are fixed during each transmission, from (10) and (11), one obtains the two-way dynamic focusing with limited-diffraction beam method developed previously (see (42), (43), and Fig. 13 of [27]) [26], [28]:

$$F_{BL}(k_x', k_y', k_z') = c^2H(k)\tilde{R}_{k_x',k_z',k_z'}(\omega), \quad (21)$$

where:

$$\begin{cases} k_x' = 2k_x \\ k_y' = 2k_y \\ k_z' = 2k_z \geq 0 \end{cases}, \quad (22)$$

which represents an increased Fourier domain coverage resulting in a higher image resolution. The increased Fourier domain coverage may be equivalent to a dynamic focusing in both transmission and reception in theory. Choosing both k_x and k_y on rectangular grids, one does not need to do any interpolation in the spatial Fourier domain of the object function along these directions. This method

also increases the image field of view as compared to the high-frame rate imaging method [27]. However, because only one line in the Fourier domain is obtained from each transmission, this method may be slow for 3-D imaging. In addition, to reconstruct an image of a large field of view, the sampling interval of both k_x and k_y must be small, which may further increase the number of transmissions needed.

3. Spherical Coordinates Approach: Using spherical coordinates for (4) or the transmission wave vector, $\vec{K}^T = (k_{x_T}, k_{y_T}, k_{z_T})$, one obtains (see (8) and Fig. 2 of [27]):

$$\begin{cases} k_{x_T} = k\sin\zeta_T\cos\theta_T = k_{1_T}\cos\theta_T \\ k_{y_T} = k\sin\zeta_T\sin\theta_T = k_{1_T}\sin\theta_T \\ k_{z_T} = k\cos\zeta_T = \sqrt{k^2 - k_{1_T}^2} \geq 0 \end{cases}, \tag{23}$$

where ζ_T is the Axicon angle [86], [87] of X wave [44], [45] or the steering angle of a plane wave, θ_T is an angle that determines components of the transmission wave vector in both x_1 and y_1 axes (for a given transmission, both ζ_T and θ_T are fixed), and:

$$k_{1_T} = k\sin\zeta_T = \sqrt{k_{x_T}^2 + k_{y_T}^2} \tag{24}$$

is the magnitude of the transverse component of the wave vector in (x_1, y_1).

Let $k_x = k_{x_T} = k\sin\zeta_T\cos\theta_T$ and $k_y = k_{y_T} = k\sin\zeta_T\sin\theta_T$, where both ζ_T and θ_T are fixed for each transmission, the Fourier space of the object function can be filled up in spherical coordinates, $(2k, \zeta_T, \theta_T)$. That is, for each plane wave transmission, echo signal is received with a plane wave response from the same direction. From (10) and (11), one obtains (21) with the following parameters for 3-D imaging:

$$\begin{cases} k_x' = 2k\sin\zeta_T\cos\theta_T \\ k_y' = 2k\sin\zeta_T\sin\theta_T \\ k_z' = k_z + k_{z_T} = 2k\cos\zeta_T \geq 0 \end{cases}, \tag{25}$$

Soumekh [67] has obtained a similar result from a linear system modeling approach in polar coordinates for 2-D imaging. Because the samples in the spatial Fourier domain are very sparse for a larger k [see (25)], a large number of transmissions at different angles are required to obtain high-frequency components accurately. Compared to the two-way dynamic focusing with limited diffraction beam approach, more transmissions may be needed to give an adequate coverage of the Fourier space.

4. Limited-Diffraction Array Beams: If the four limited-diffraction array beams in (26)–(29) (see next page) [29], [32], [61], [62] are transmitted (fix both k_{x_T} and k_{y_T} for each transmission) one obtains four coverage areas in the spatial Fourier space of $f(\vec{r}_0)$ from combinations of the four echo signals. Denoting the Fourier transform of the four echo signals as $\tilde{R}^{(1)}_{k_x',k_y',k_z'}(\omega)$, $\tilde{R}^{(2)}_{k_x',k_y',k_z'}(\omega)$, $\tilde{R}^{(3)}_{k_x',k_y',k_z'}(\omega)$, and $\tilde{R}^{(4)}_{k_x',k_y',k_z'}(\omega)$, corresponding to (26)–(29), respectively, one has (30)–(33) (see next page).

Changing k_{x_T} and k_{y_T}, one obtains partially overlapped coverage of the spatial Fourier domain because k_x and k_y are free to change; (11) can be used to perform the mapping between the echo Fourier domain and the Fourier domain of the object function for each transmission, and the mapping will be discussed in the next section. Superposing the partially reconstructed images in spatial domain or their spectra in the spatial Fourier domain from different transmissions, one obtains the final image with (17). The superposition in spatial domain can be done either coherently (increase image resolution and contrast) or incoherently (reduce speckles) [59], [60]. In frequency domain, the superposition can be done only coherently, which in theory is equal to the superposition in the spatial domain. The superposition also will increase the field of view of the final image [59], [60].

5. Steered Plane Waves: As discussed previously, (10) and (11) directly give a relationship between the 3-D Fourier transform of measured echo signals at the transducer surface and the 3-D spatial Fourier transform of the object function for a steered plane wave transmission with fixed Axicon angle (steering angle for plane waves), ζ_T, [86], [87] of X wave [44], [45] and azimuthal angle, θ_T. (See spherical coordinates approach above.) After getting the spatial Fourier transform of the object function, using (17) one can reconstruct images with an inverse 3-D Fourier transform. In the reconstruction, the same superposition schemes described above in the section of limited diffraction array beams can be used. The partially reconstructed images for each fixed pair of ζ_T and θ_T in either spatial Fourier or spatial domain can be used to increase image resolution, contrast, field of view, or reduce speckle noises.

In addition to the earlier work in [27], [28], [59], [60], Liu also considered steering plane waves to obtain a large field of view, increasing image resolution or reducing speckles [88]. Using the zeroth-order Hankel function, Liu derived a relationship between the Fourier transform of echoes and the Fourier transform of an object function for 2-D imaging. From (13)–(16), it is clear that the relationship derived by Liu is a special case of (15) of [27] or a special case of (10) [for 2-D imaging, one can simply set $k_y = k_{y_T} = 0$ in (10) and (11)].

For steered plane waves, one obtains the relationship of the parameters between the Fourier transform of the echoes and the object function [see (11) and (23)]:

$$\begin{cases} k_x' = k_x + k\sin\zeta_T\cos\theta_T \\ k_y' = k_y + k\sin\zeta_T\sin\theta_T \\ k_z' = k_z + k\cos\zeta_T = \sqrt{k^2 - k_x^2 - k_y^2} + k\cos\zeta_T \geq 0 \end{cases}, \tag{34}$$

$$\Phi^T_{\text{Array}(1)}(\vec{r}_0,t)=\frac{1}{2\pi}\int_{-\infty}^{\infty}A(k)H(k)\cos\left(k_{x_T}x_0\right)\cos\left(k_{y_T}y_0\right)e^{ik_{z_T}z_0}e^{-i\omega t}dk, \tag{26}$$

$$\Phi^T_{\text{Array}(2)}(\vec{r}_0,t)=\frac{1}{2\pi}\int_{-\infty}^{\infty}A(k)H(k)\cos\left(k_{x_T}x_0\right)\sin\left(k_{y_T}y_0\right)e^{ik_{z_T}z_0}e^{-i\omega t}dk, \tag{27}$$

$$\Phi^T_{\text{Array}(3)}(\vec{r}_0,t)=\frac{1}{2\pi}\int_{-\infty}^{\infty}A(k)H(k)\sin\left(k_{x_T}x_0\right)\cos\left(k_{y_T}y_0\right)e^{ik_{z_T}z_0}e^{-i\omega t}dk, \tag{28}$$

and:

$$\Phi^T_{\text{Array}(4)}(\vec{r}_0,t)=\frac{1}{2\pi}\int_{-\infty}^{\infty}A(k)H(k)\sin\left(k_{x_T}x_0\right)\sin\left(k_{y_T}y_0\right)e^{ik_{z_T}z_0}e^{-i\omega t}dk, \tag{29}$$

$$F_{BL}\left(k_x+k_{x_T},k_y+k_{y_T},k_z+k_{z_T}\right)=c^2H(k)\left(\tilde{R}^{(1)}_{k'_x,k'_y,k'_z}(\omega)+i\tilde{R}^{(2)}_{k'_x,k'_y,k'_z}(\omega)+i\tilde{R}^{(3)}_{k'_x,k'_y,k'_z}(\omega)-\tilde{R}^{(4)}_{k'_x,k'_y,k'_z}(\omega)\right), \tag{30}$$

$$F_{BL}\left(k_x+k_{x_T},k_y-k_{y_T},k_z+k_{z_T}\right)=c^2H(k)\left(\tilde{R}^{(1)}_{k'_x,k'_y,k'_z}(\omega)-i\tilde{R}^{(2)}_{k'_x,k'_y,k'_z}(\omega)+i\tilde{R}^{(3)}_{k'_x,k'_y,k'_z}(\omega)+\tilde{R}^{(4)}_{k'_x,k'_y,k'_z}(\omega)\right), \tag{31}$$

$$F_{BL}\left(k_x-k_{x_T},k_y+k_{y_T},k_z+k_{z_T}\right)=c^2H(k)\left(\tilde{R}^{(1)}_{k'_x,k'_y,k'_z}(\omega)+i\tilde{R}^{(2)}_{k'_x,k'_y,k'_z}(\omega)-i\tilde{R}^{(3)}_{k'_x,k'_y,k'_z}(\omega)+\tilde{R}^{(4)}_{k'_x,k'_y,k'_z}(\omega)\right), \tag{32}$$

$$F_{BL}\left(k_x-k_{x_T},k_y-k_{y_T},k_z+k_{z_T}\right)=c^2H(k)\left(\tilde{R}^{(1)}_{k'_x,k'_y,k'_z}(\omega)-i\tilde{R}^{(2)}_{k'_x,k'_y,k'_z}(\omega)-i\tilde{R}^{(3)}_{k'_x,k'_y,k'_z}(\omega)-\tilde{R}^{(4)}_{k'_x,k'_y,k'_z}(\omega)\right). \tag{33}$$

C. 2-D High-Frame Rate Imaging Theory

Eq. (10) and (11) give a general 3-D image reconstruction formula that is similar to (15) of [27]. They are readily suitable for 2-D image reconstructions. Setting one of the transverse coordinates, say, $k_y = k_{y_T} = 0$, one obtains a 2-D imaging formula (see (34) of [27]):

$$F_{BL}(k'_x,k'_z)=c^2H(k)\tilde{R}_{k'_x,k'_z}(\omega), \tag{35}$$

where

$$\begin{cases} k'_x=k_x+k_{x_T} \\ k'_z=k_z+k_{z_T}=\sqrt{k^2-k_x^2}+\sqrt{k^2-k_{x_T}^2}\geq 0 \end{cases}, \tag{36}$$

Eq. (35) and (36) are the equations for reconstructions of images from data obtained with simulations and experiments.

III. Relationships Between Fourier Domains of Echoes and Object Function

To reconstruct images with FFT, it is necessary to obtain the Fourier transform of the object function at rectangular grids of (k'_x,k'_y,k'_z). However, the Fourier transform of echo data is known only on rectangular grids of (k_x,k_y,k), which is related to (k'_x,k'_y,k'_z) by (11). In this section, mapping of data with (11) will be given for two special cases (limited-diffraction array beam and steered plane wave transmissions) for 2-D imaging. They will be used in the reconstruction of images in both simulations and experiments in later sections. Mappings for other special cases and for 3-D can be done similarly.

A. Image Reconstruction with Limited-Diffraction Array Beams

For limited-diffraction array beams, an inverse function of (36) can be derived:

$$\begin{cases} k_x=k'_x-k_{x_T} \\ k=\dfrac{\sqrt{\left(k_z'^2+k_{x_T}^2-\left(k'_x-k_{x_T}\right)^2\right)^2+4k_z'^2\left(k'_x-k_{x_T}\right)^2}}{2k'_z} \end{cases}. \tag{37}$$

To exclude evanescent waves, both $|k_x|\leq k$ and $|k_{x_T}|\leq k$ must be satisfied in (36) (where $k\geq 0$). For limited diffraction array beam weighting, k_{x_T} is a constant in each transmission. This means that the aperture weighting function is the same for all the frequency components, k, in each transmission. From these conditions, one set of

boundaries in (k'_x, k'_z) can be found by setting $k_x = k$ or $k_x = -k$ in (36):

$$(k'_x - k_{x_T})^2 - k_z'^2 = k_{x_T}^2, \text{ if } k_x = k \text{ or } k_x = -k, \tag{38}$$

which is a hyperbolic function with its center shifted to $(k_{x_T}, 0)$. The hyperbolic function has two branches that intersect with k'_x axis at two points, i.e., at $k'_x = 0$ and $k'_x = 2k_{x_T}$, respectively. Another boundary can be found by setting $k_{x_T} = k$ or $k_{x_T} = -k$ in (36), which gives a half circle centered at $(k_{x_T}, 0)$ with a radius of $|k_{x_T}|$ that intercepts with the hyperbolic curves at $(0, 0)$ and $(0, 2k_{x_T})$ respectively:

$$(k'_x - k_{x_T})^2 + k_z'^2 = k_{x_T}^2, \text{ if } k_{x_T} = k \text{ or } k_{x_T} = -k. \tag{39}$$

If the imaging system is band limited (i.e., $k_{\min} \le k \le k_{\max}$), from (36) another two circular boundaries can be obtained:

$$(k'_x - k_{x_T})^2 + \left(k'_z - \sqrt{k_{\min}^2 - k_{x_T}^2}\right)^2 = k_{\min}^2, \quad \text{if } k = k_{\min} \ge k_{x_T}, \tag{40}$$

and

$$(k'_x - k_{x_T})^2 + \left(k'_z - \sqrt{k_{\max}^2 - k_{x_T}^2}\right)^2 = k_{\max}^2, \quad \text{if } k = k_{\max} \ge k_{x_T}, \tag{41}$$

which further limit the size of the mapping area in (k'_x, k'_z). As k_{x_T} increases, low-frequency components cannot be transmitted to illuminate objects, which could lower the energy efficiency. Outside of the boundaries, values at (k'_x, k'_z) are simply set to 0 [Fig. 2(a) and (b)]. The mapping can be done with bilinear interpolation. To increase the interpolation accuracy, data in the Fourier domain of echoes can be densified by zero padding as long as the original data are not aliased.

For limited-diffraction array beam transmissions, both sine and cosine weightings are applied; thus the echoes need to be combined using a 2-D version of (30)–(33) to get two new sets of echoes before the mapping process above. The combination could be done in either echo or echo Fourier domain. Images can be reconstructed from the mapped data [see the text below (33)].

B. Image Reconstruction with Steered Plane Waves

Images also can be reconstructed with steered plane waves. To steer a plane wave, linear time delays are applied to transducer elements:

$$\tau(x_1) = -x_1 \sin\zeta_T / c, \tag{42}$$

where $x_1 \in (-D/2, D/2)$ is the position of the center of an element of an array transducer, D is the size of the transducer aperture, and ζ_T is the steering angle that is fixed for each transmission. To make the system causal, an additional constant delay may be added to the delay function (42).

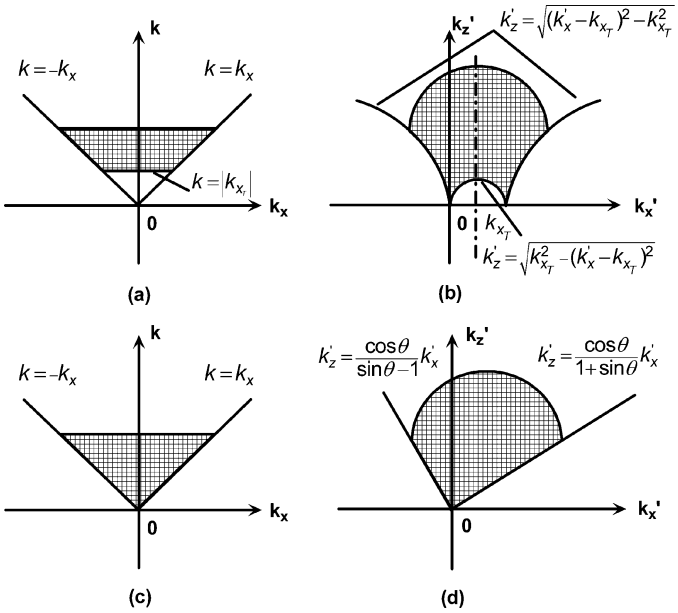

Fig. 2. Mapping between the Fourier transform of echo signals (a) and (c) and the Fourier transform of an object function (b) and (d), for limited-diffraction array beam (a) and (b) and steered plane wave (c) and (d) transmissions. (Notice that (b) and (d) are similar to the Ewald sphere [81]. However, the data acquisition techniques and thus the Fourier domain coverage in [81] are different from those in the current paper.) Note that θ in this figure is ζ_T in (44).

Assuming $k_{x_T} = k \sin\zeta_T$, from (36) or a 2-D case of (34), one obtains an inverse function:

$$\begin{cases} k_x = k'_x - k\sin\zeta_T \\ k = \frac{k_z'^2 + k_x'^2}{2k'_z\cos\zeta_T + 2k'_x\sin\zeta_T} \end{cases}. \tag{43}$$

To exclude evanescent waves, the condition for steered plane waves is $|k_x| \le k$ (notice that $k \ge 0$ and $|\zeta_T| < \pi/2$). With this condition, one set of boundaries in (k'_x, k'_z) can be determined by setting $k_x = k$ and $k_x = -k$, respectively, in (36):

$$\begin{cases} k'_z = \frac{\cos\zeta_T}{\sin\zeta_T + 1} k'_x, & \text{if } k_x = k \\ k'_z = \frac{\cos\zeta_T}{\sin\zeta_T - 1} k'_x, & \text{if } k_x = -k \end{cases}. \tag{44}$$

If the imaging system is band limited (i.e., $k_{\min} \le k \le k_{\max}$), another two boundaries can be added using (36) and $k_{x_T} = k\sin\zeta_T$:

$$\begin{cases} (k'_x - k_{\min}\sin\zeta_T)^2 + (k'_z - k_{\min}\cos\zeta_T)^2 = k_{\min}^2, \\ \text{if } k_x = k_{\min} \\ (k'_x - k_{\max}\sin\zeta_T)^2 + (k'_z - k_{\max}\cos\zeta_T)^2 = k_{\max}^2, \\ \text{if } k_x = k_{\max} \end{cases}. \tag{45}$$

Outside of the boundaries, values at (k'_x, k'_z) are simply set to 0 [see Fig. 2(c) and (d)]. Similar to the limited-diffraction array beam case, the mapping can be done with

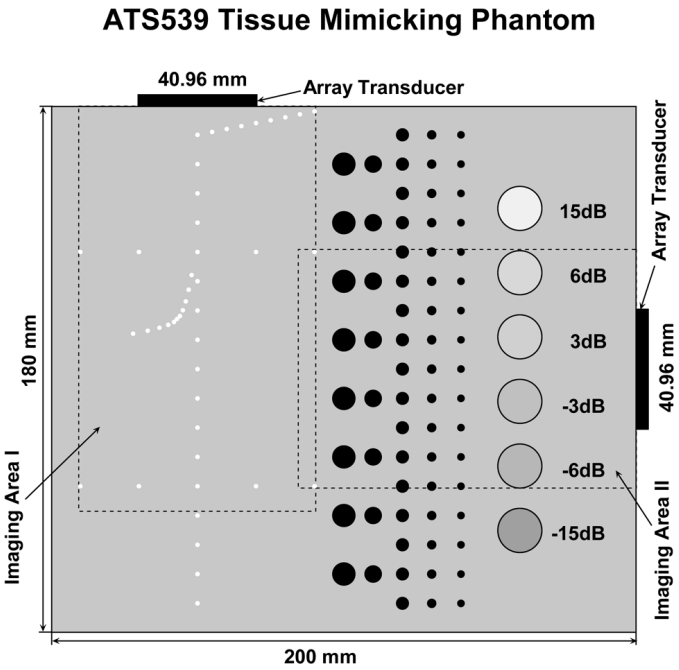

Fig. 3. Structure and imaging areas of an ATS539 multipurpose tissue-mimicking phantom.

the bilinear interpolation. To increase the interpolation accuracy, data in the Fourier domain of echoes can be densified with zero padding as long as the original data are not aliased.

IV. Computer Simulation

To verify the extended high frame rate (HFR) imaging theory in ideal conditions, computer simulations were performed. For simplicity, only 2-D imaging will be considered. The simulation algorithms are developed based on the impulse response methods [89]–[93].

In the simulations, a 128-element, 1-D linear array transducer of 3.5 MHz center frequency and 58% −6 dB pulse-echo fractional bandwidth defined by the square of the Blackman window function [44] is assumed. A one-cycle sine wave pulse at the center frequency of the transducer is used to excite the transducer. The dimensions of the transducer are 0.32 mm (pitch), 8.6 mm (elevation width), and 40.96 mm (aperture length), respectively. The pitch is about three-fourths of the center wavelength of the transducer. There is no elevation focus for the transducer.

Two objects are used in the simulations. One is based on the wire pattern of the ATS539 (ATS Laboratories, Inc., Bridgeport, CT) multipurpose tissue-mimicking phantom (see imaging Area I and the position of the transducer in Fig. 3). There are 40-wire targets in this imaging area, each wire is represented with a point scatterer, and all point scatterers are assumed to have the same scattering coefficient. The second object consists of 18 point-scatterers of the same scattering coefficient. The point scatterers are aligned along three lines with six point-scatterers in each line, evenly spaced with 20-mm spacing. The first line is perpendicular to the transducer surface, and the other two are at 15 and 30 degrees from the first line, respectively. The center of the transducer is aligned with the first line. The geometry of the object is the same as that of the reconstructed images to be described later, except that the points in the reconstructed images are not exactly geometrical points.

Reconstructed images of the first object are shown in Figs. 4 and 5 with limited-diffraction array beams and steered plane waves in transmissions, respectively. In each figure, there are four panels for images reconstructed with one transmission (up to 5500 frames/second with a speed of sound of 1540 m/s) [Figs. 4(a) and 5(a)], 11 transmissions (up to 500 frames/second) [Figs. 4(b) and 5(b)], 91 transmissions (up to 60 frames/second) [Figs. 4(c) and 5(c)], and 263 transmissions (up to 21 frames/second) [Figs. 4(d) and 5(d)], respectively, for a depth of 140 mm. As a comparison, panels Figs. 4(d) and 5(d) are the same and are obtained with the conventional delay-and-sum method with its transmission focus at 70 mm.

For limited-diffraction array beam transmissions, the maximum value of k is calculated with $k_{x_T\_\max} = \pi/\Delta x_1$, where Δx_1 is the pitch of the transducer. Because both sine and cosine aperture weightings are needed for each k_{x_T}, a total of 46, 6, and 1 k_{x_T}, equally spaced from 0 to $k_{x_T\_\max}$, are used to produce the results with 91, 11, and 1 transmissions, respectively (for 1 transmission, $k_{x_T} = 0$). For steered plane waves, 91, 11, and 1 transmissions, evenly spaced with the condition $|\zeta_T| \leq \pi/4$, are used to produce the results (for 1 transmission, $\zeta_T = 0$). For conventional delay-and-sum method, the following formula is used to obtain the evenly spaced sine of the steering angles (there are less transmissions at larger angles than at smaller ones):

$$\sin\theta_n = n(\lambda_0/2)/D, \quad n = 0, \pm 1, \pm 2, \ldots, \pm(N-1)/2, \tag{46}$$

where θ_n is nth-steering angle, λ_0 is the center wavelength, D is the aperture size of the transducer. For θ_n to cover $\pm 45°$, with an assumption of the speed of sound of 1540 m/s, one obtains $N = 263$.

For 91 transmissions, it is seen from Figs. 4 and 5 that image resolution is high and sidelobe is low (images are log-compressed in 50 dB) for both limited-diffraction array beam and steered plane wave transmissions as compared to the conventional delay-and-sum method. Even with one transmission, the results are still comparable to that of delay-and-sum except near the transmission focal depth. The results for limited-diffraction array beam and steered plane wave transmissions are similar, except the former has a somewhat higher resolution.

Simulations with the second object are done to compare the image quality of both limited-diffraction array beam and steered plane wave transmissions with the conventional delay-and-sum method of transmission focusing at all depths (dynamic transmission focusing) (Fig. 6). For delay-and-sum method, dynamic focusing in transmission

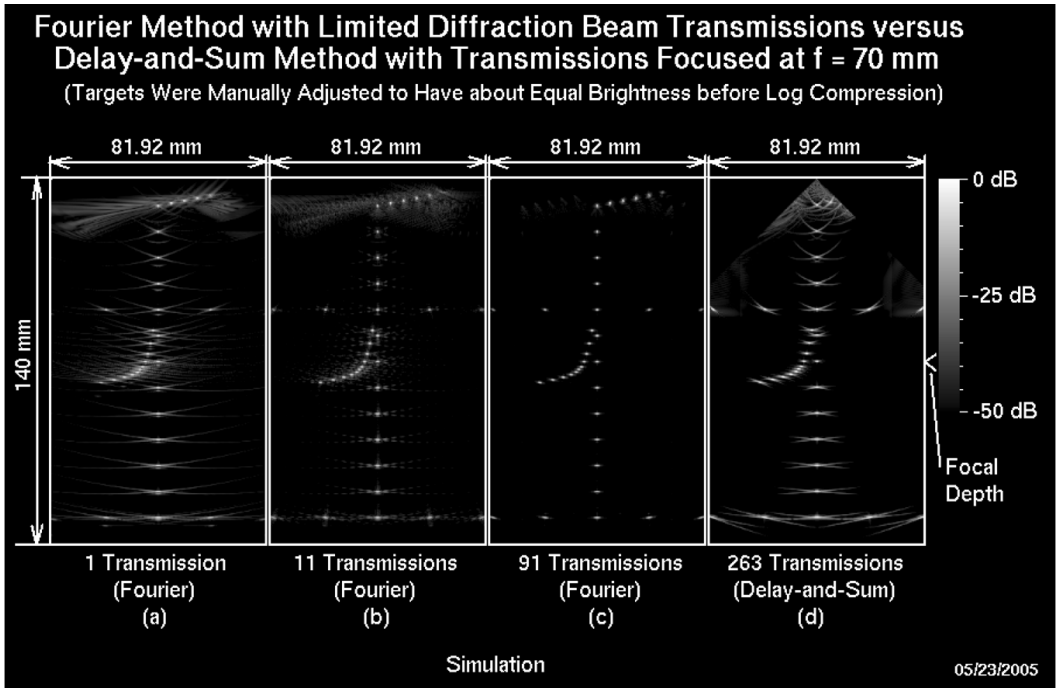

Fig. 4. Simulated images according to the imaging area I of the ATS539 phantom (see Fig. 3). Images are reconstructed with limited-diffraction array beam transmissions. Images are log-compressed at 50 dB. The transducer has 128 elements, 40.96-mm aperture, 0.32-mm pitch, 3.5-MHz center frequency, and 58% −6 dB pulse-echo bandwidth. The area of each image panel is 81.92 × 140 mm. Images are obtained with (a) 1 (up to 5500 frames/second with 1540 m/s speed of sound), (b) 11 (up to 500 frames/second), and (c) 91 (up to 60 frames/second) transmissions, respectively. (d) Result obtained with the conventional delay-and-sum method with a fixed transmission focal depth of 70 mm and with 263 transmissions (up to 21 frames/second).

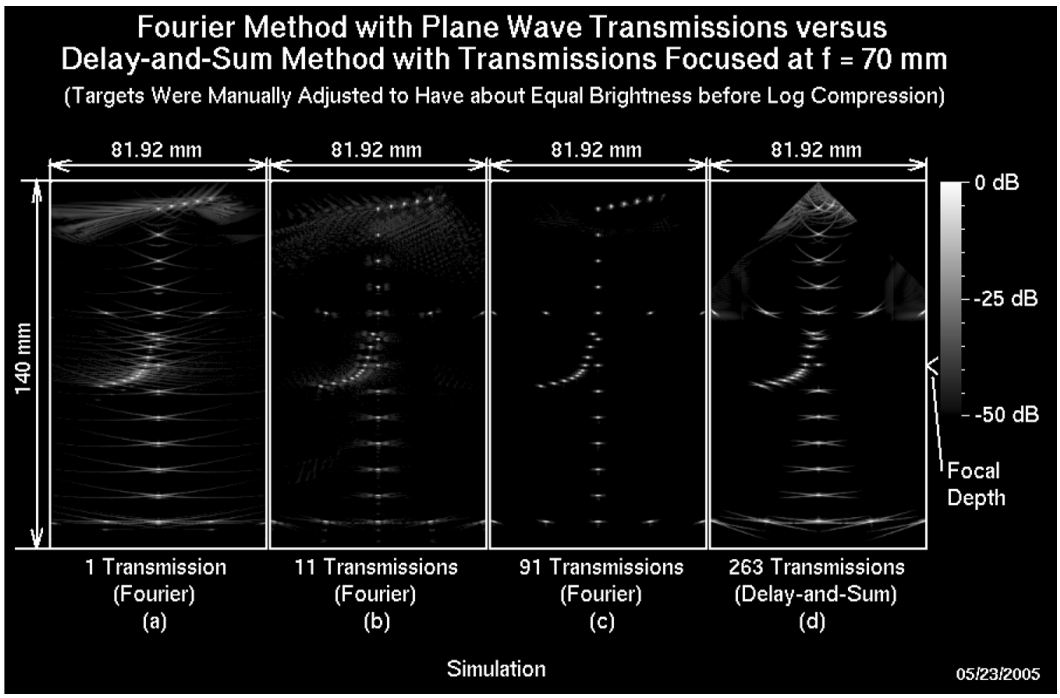

Fig. 5. The same as Fig. 4 except that steered plane waves are used in transmissions instead of limited-diffraction array beams.

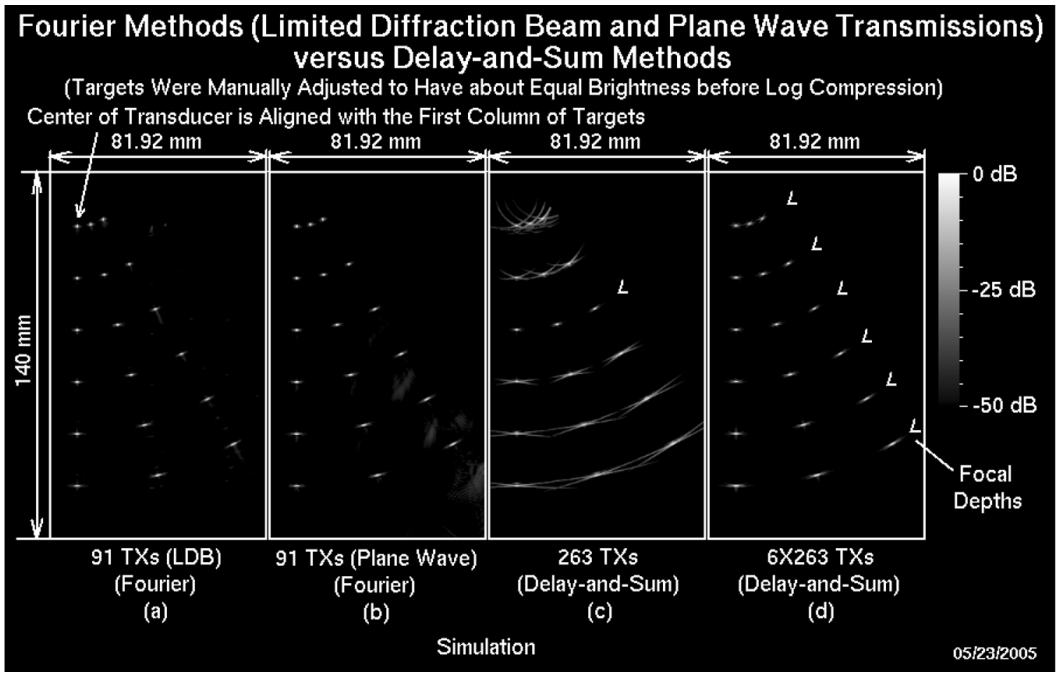

Fig. 6. Simulated images for 18 point scatterers on three lines with 15 degrees between the lines. Six point scatterers are distributed evenly over each line with 20-mm spacing. The log compression, image panel size, and parameters of the transducer are the same as those in Fig. 4. Image reconstructed with: (a) Limited-diffraction array beam transmissions (91 transmissions up to 59 frames/second). (b) Steered plane wave transmissions. (c) Delay-and-sum method with a fixed focal depth at 60 mm (263 transmissions up to 20 frames/second). (d) Delay-and-sum method with a dynamically focused transmission synthesized using a montage process.

is achieved with a montage process, i.e., cutting a strip of each reconstructed image around its focal distance, then piecing all the strips together to form a synthesized image. Apparently, this process lowers image frame rate dramatically. Despite the added complexity and a low-frame rate, the resolution of the delay-and-sum method with the montage process [Fig. 6(d)] is lower than that of either limited-diffraction array beam [Fig. 6(a)] or steered plane wave [Fig. 6(b)] method with 91 transmissions. The delay-and-sum method with a fixed transmission focus [Fig. 6(c)] has the worst result. It should be mentioned that both limited-diffraction array beam and steered plane wave methods have high computation efficiency due to the use of FFT (the difference is on how to transmit—sine and cosine weighting are used to produce limited-diffraction array beams, and linear-time delay is used to produce a steered plane wave).

V. In Vitro and In Vivo Experiments

To test the extended HFR imaging theory in practical situations, both *in vitro* and *in vivo* experiments are carried out with a homemade HFR imaging system [62], [77], [78].

A. Experiment System and Experiment Conditions

A HFR imaging system [62], [77], [78] was designed and constructed in our lab and was used for all the experiments. This system has 128 independent, wideband (0.05 MHz–10 MHz) arbitrary waveform generators (power amplifiers), and each of them has a 40 MHz 12-bit D/A as its input and produces up to ±144 V output at a 75 Ω load. The system also has 128 independent receiving channels, and each has a low-noise, time-gain-control (TGC) amplifier of up to 108 dB gain and 10 MHz bandwidth (0.25 MHz–10 MHz). Each channel also has a 12-bit A/D of 40 MHz sampling rate and a SDRAM of up to 512 MB for storing digitized echo signals. Data are transferred through a USB 2.0 (high-speed) link to a computer for image reconstruction. The system operation is controlled by the computer using the same USB link.

In the experiment, a one-cycle sine wave at the center frequency of the transducer is used to excite the transducer. For limited-diffraction array beam transmissions, array transducers are weighted with either sine or cosine function of different parameters, k_{x_T}. For steered plane wave or conventional delay-and-sum methods, linear time delays are applied to the transducers to steer the beams. The precision of the time delay of the system is 6.25 ns, which is determined by a 160 MHz clock. In receive mode, signals are digitized at the same time at a 40 MHz sampling rate. During image reconstruction, signals can be down sampled to 10 MHz for both limited-diffraction array beam and steered plane wave methods. However, the delay-and-sum method requires 40 MHz to ensure image reconstruction quality.

B. In Vitro Experiments

In the *in vitro* experiments, the same array transducer as in the simulations is used, except that the real trans-

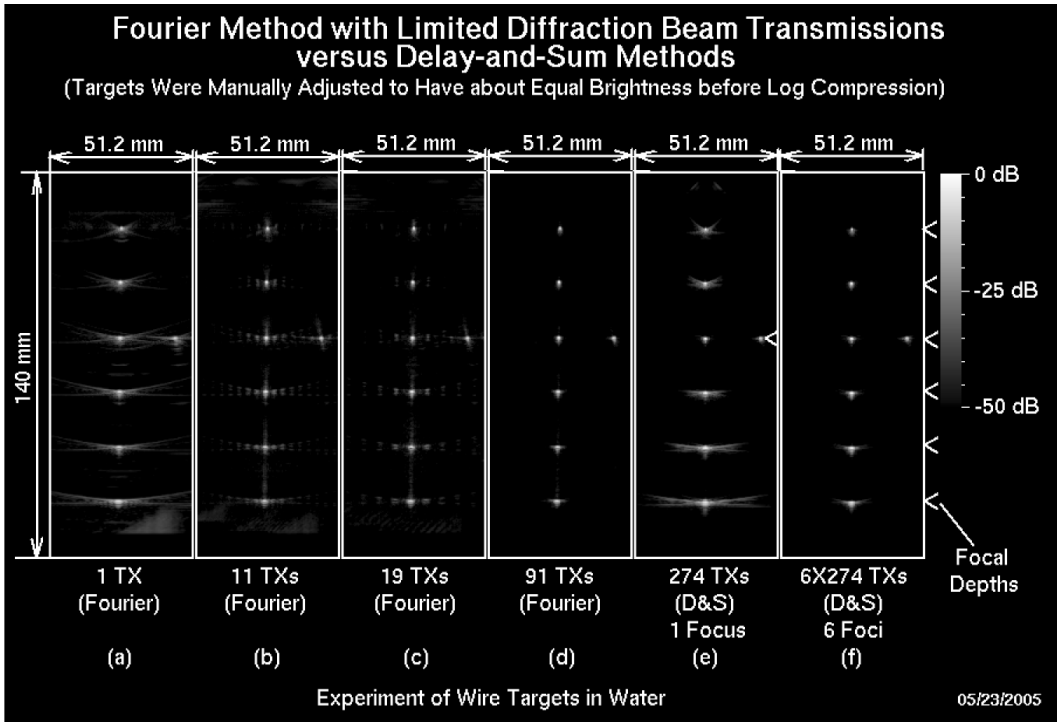

Fig. 7. Experiment results of a wire phantom in water. Images are reconstructed with limited-diffraction array beam transmissions. There are seven wires in total with six wires in a line and one wire on the third row 20 mm to the right of the line. The image panel size is 51.2×140 mm. The six wires are evenly distributed with 20-mm spacing. The log compression and the parameters of the transducer are the same as those in Fig. 4, except that the -6 dB pulse-echo bandwidth of the transducer is about 50% instead of 58% of the center frequency. Images are obtained with: (a) 1 (up to 5277 frames/second, with 1477.56 m/s speed of sound); (b) 11 (up to 479 frames/second); (c) 19 (up to 278 frames/second); and (d) 91 (up to 58 frames/second) transmissions, respectively. (e) Result obtained with the delay-and-sum method with a fixed transmission focal depth of 60 mm and with 274 transmissions (up to 19 frames/second); and (f) result of the delay-and-sum method with a dynamically focused transmission synthesized with a montage process.

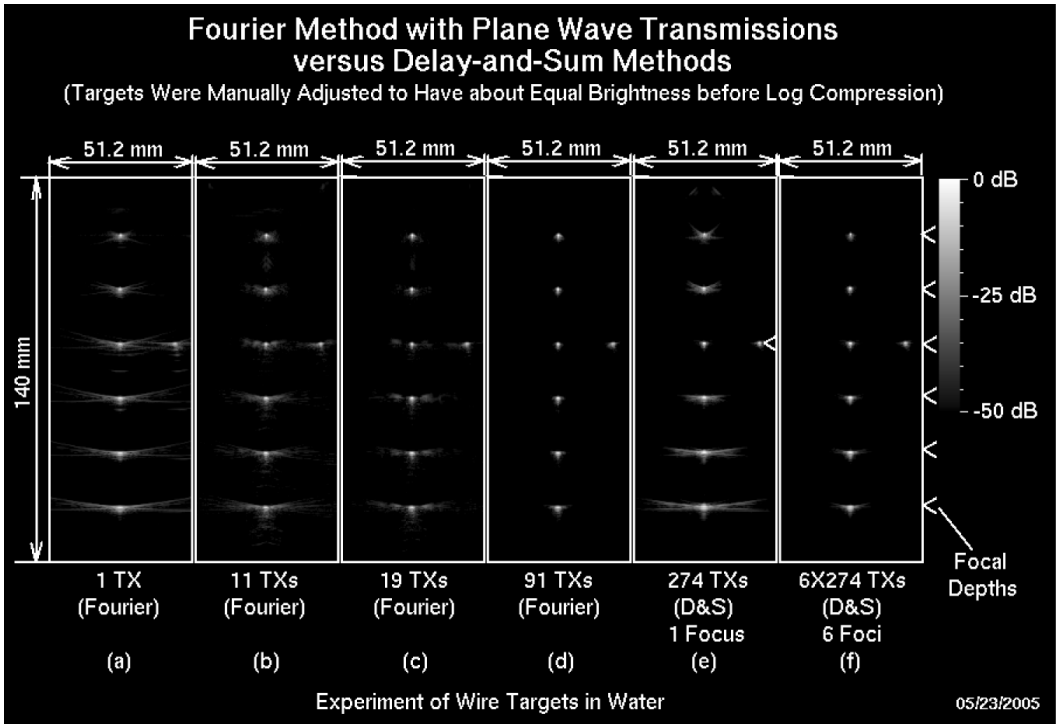

Fig. 8. The same as Fig. 7, except that steered plane waves are used in transmissions instead of limited-diffraction array beams.

ducer has a bandwidth of about 50% instead of 58% of the center frequency. Other imaging parameters for the experiments are also the same as those in simulations. To show the line spread function of the imaging methods, a homemade wire phantom consisting of six nylon wires (0.25 mm in diameter) in a line with an inter-wire spacing of 20 mm is used and images reconstructed with limited-diffraction array beam and steered plane wave transmissions are shown in Figs. 7 and 8, respectively. (There is one more wire in the third row of both figures that is 20 mm away from the line.) To show how image frame rate trades off with improved image quality (see both Figs. 7 and 8), results for 1 [up to 5277 frames/second with a speed of sound of 1477.56 m/s, panel (a)], 11 (up to 479 frames/second, panel (b)], 19 [up to 278 frames/second, panel (c)], and 91 [up to 58 frames/second, panel (d)] transmissions are obtained. For comparison, results of conventional delay-and-sum method with a fixed transmission focus of 60 mm and synthesized dynamic transmission focusing with montage are shown in panel (e) and (f), respectively (see Figs. 7 and 8). In the experiment, the temperature in water tank is about 18.5°C and thus the speed of sound is about 1477.56 m/s [94]. According to (46), this gives the number of transmissions of 274 (up to 19 frames/second) for a fixed focus delay-and-sum method. The experiment results are very similar to those of simulations.

Experiment results of the imaging area I (see Fig. 3) of the ATS539 multifunction tissue-mimicking phantom are shown in Figs. 9 and 10, respectively. The phantom has 0.5 dB/cm/MHz attenuation and the speed of sound is 1450 m/s. The line targets of the monofilament nylon have a diameter of 0.12 mm. The results are similar to those obtained in the computer simulations (compare Figs. 9 and 10 with Figs. 4 and 5, respectively).

The ATS539 phantom also contains anechoic cylindrical cysts with diameters of 2, 3, 4, 6, and 8 mm, respectively. In addition, there are six 15-mm diameter grayscale cylindrical targets, with their contrasts to background of +15, +6, +3, −3, −6, and −15 dB, respectively. Experiment results of imaging area II (see Fig. 3) are shown in Figs. 11 and 12, respectively, for limited-diffraction array beam and steered plane wave transmissions (with 1, 11, and 91 transmissions). For comparison, image with delay-and-sum method with a focal depth of 70 mm is shown in panel (d) of both Figs. 11 and 12. It is seen that, as the number of transmissions increases, image contrast is increased significantly for both limited-diffraction array beam and steered plane wave transmissions. Because the noise of the HFR imaging system is relatively high, the contrast of cystic targets is lowered because the noise fills into the cystic areas. This is more acute for limited-diffraction array beam transmissions in which the sine or cosine weightings further reduce the transmission power by half [62]. In addition, when k_{x_T} is fixed in a limited-diffraction array beam transmission, a lower transmission frequency may have a larger spreading angle further reducing energy density, although the image field of view could be increased. Furthermore, with a large k_{x_T}, low frequency components become evanescent waves and cannot be transmitted. Nonetheless, limited-diffraction array beam transmissions may simplify the transmitters because there is no time or phase delay that is needed to steer the beam and may have other advantages as mentioned in Section I [62].

C. In Vivo Experiments

In the *in vivo* experiments, an Acuson V2 (Acuson, Mountain View, CA) phased array transducer is used. The *in vivo* experiments are performed with the right kidney and the heart of a healthy volunteer. The transducer has 128 elements, 2.5 MHz center frequency, 19.2-mm aperture, 14-mm elevation dimension focused at 68-mm depth, and 0.15-mm pitch. Given these parameters and (46), the number of transmissions required for the delay-and-sum method is 88 (assuming the speed of sound is 1540 m/s) to cover ±45° steering angles. The transmission beam is focused at 70 mm and the imaging depth is 120 mm.

In the experiments, a commercial Acuson 128XP/10 is used for real-time feedback for operators. Once the structure of interest is found, the transducer position is fixed by a fastener, and the transducer is unplugged from the Acuson machine then plugged into the HFR imaging system for data acquisition. Data are acquired at the highest frame rate that the HFR imaging system is allowed for the depth (187 μs between transmissions or 5348 frames/second) [62]. Because of motion of the organs, to obtain images at approximately the same view for comparison, different transmission methods are programmed to follow immediately one after another. For kidney (Fig. 13), 91 steered plane wave transmissions start as soon as 88 delay-and-sum transmissions are completed. For heart (Fig. 14), the imaging sequence is that the 88 [61 frames/second, see panel (d)] delay-and-sum transmissions are finished first, followed by 11 [486 frames/second, see panel (a)], 19 [281 frames/second, see panel (b)], and 91 [59 frames/second, see panel (c)] transmissions of the steered plane wave method. The data acquisition of the heart is triggered and synchronized by an electrocardiograph (ECG) signal to get images at the desired heart cycle moments (see the ECG display on the right-hand side of Fig. 14). From both Figs. 13 and 14, it is seen that the steered plane wave with 91 transmissions produces images that are better in both resolution and contrast than the conventional delay-and-sum method of a similar number of transmissions. For the heart imaging, it is seen that the image quality can be traded off with frame rate. Motion artifacts were a concern for the extended HFR imaging theory when more than one transmission is used; however, from the *in vivo* heart images, it seems that the extended theory is not very sensitive to the motion. This is because the HFR imaging theory allows one transmission to reconstruct a complete image [27], i.e., the quality of each subimage is not affected by the motion, and the heart does not move that fast to distort the image when subimages obtained from different transmissions are superposed. In our experiment, only 91 transmissions are used. This translates into a time

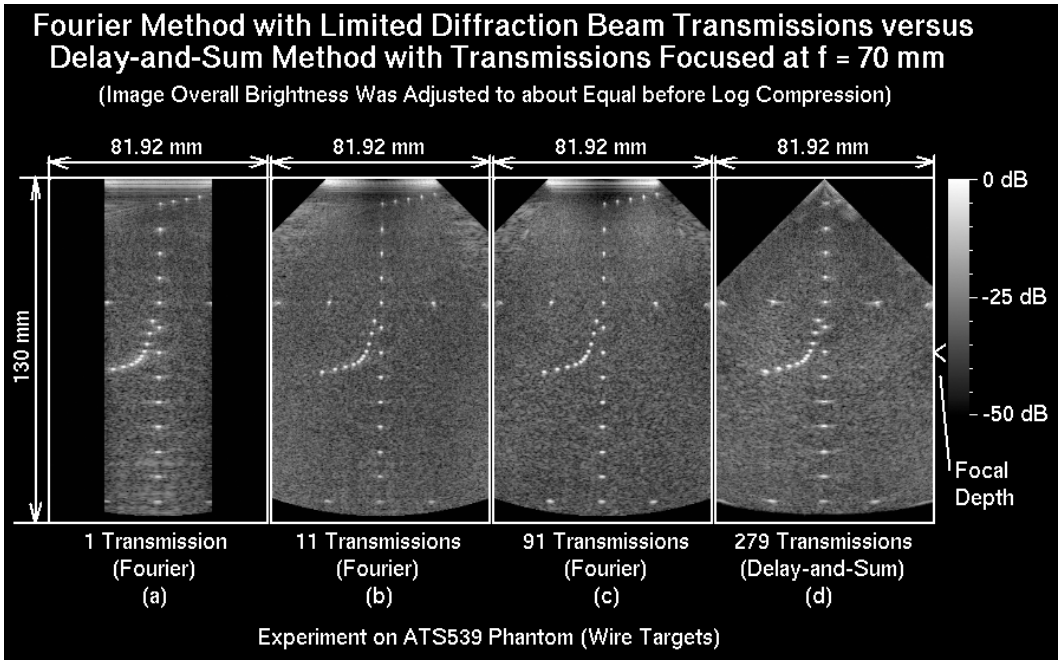

Fig. 9. The same as Fig. 4, except that these are experiment results from a real ATS539 phantom on imaging area I (see Fig. 3) using a real transducer. The speed of sound of the phantom is 1450 m/s and the −6 dB pulse-echo bandwidth of the transducer is about 50% of the center frequency.

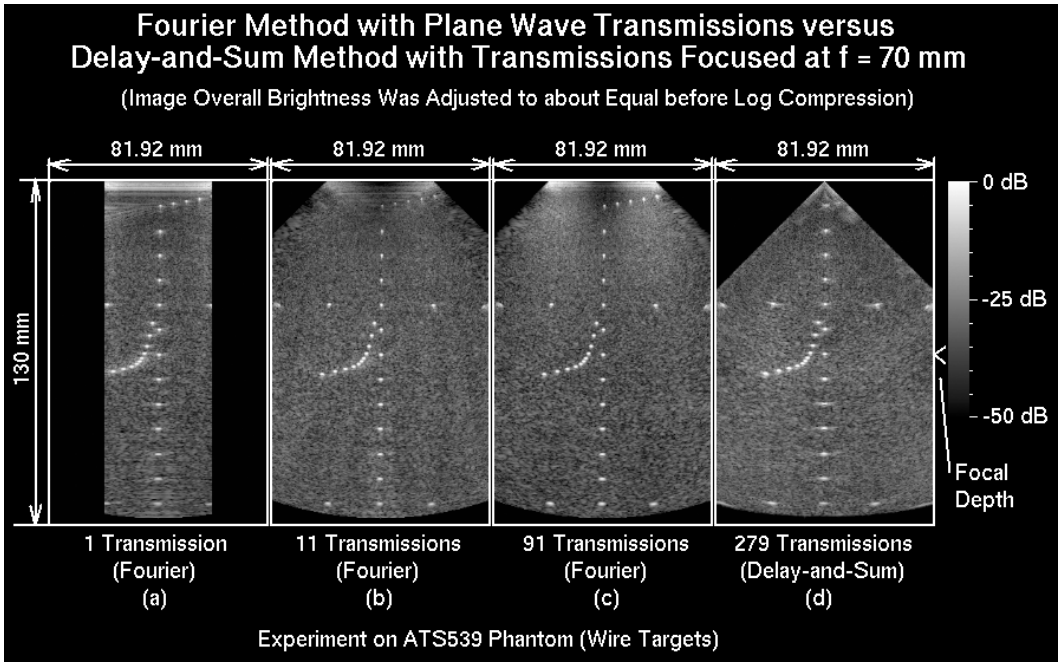

Fig. 10. The same as Fig. 9, except that steered plane waves are used in transmissions instead of limited-diffraction array beams.

span of 91×187 μs = 17.017 ms. Assuming the highest speed of the heart motion is about 0.2 m/s, the maximum registration error of subimages would be about 3.4 mm. Furthermore, at a larger distance, the image resolution is generally poor, and the subimages will not overlap after a fraction of the total number of transmissions. This makes motion artifacts less noticeable. In addition, most heart tissues move at a much lower speed than the peak velocity assumed above.

VI. Discussion

A. Fourier-Domain Coverage

As mentioned before, changing k_{x_T} and k_{y_T} in limited-diffraction array beam, or changing ζ_T in steered plane wave transmissions, one obtains partially overlapped coverage of the spatial Fourier domain because k_x and k_y are free to change [see (11)]. Superposing the partially recon-

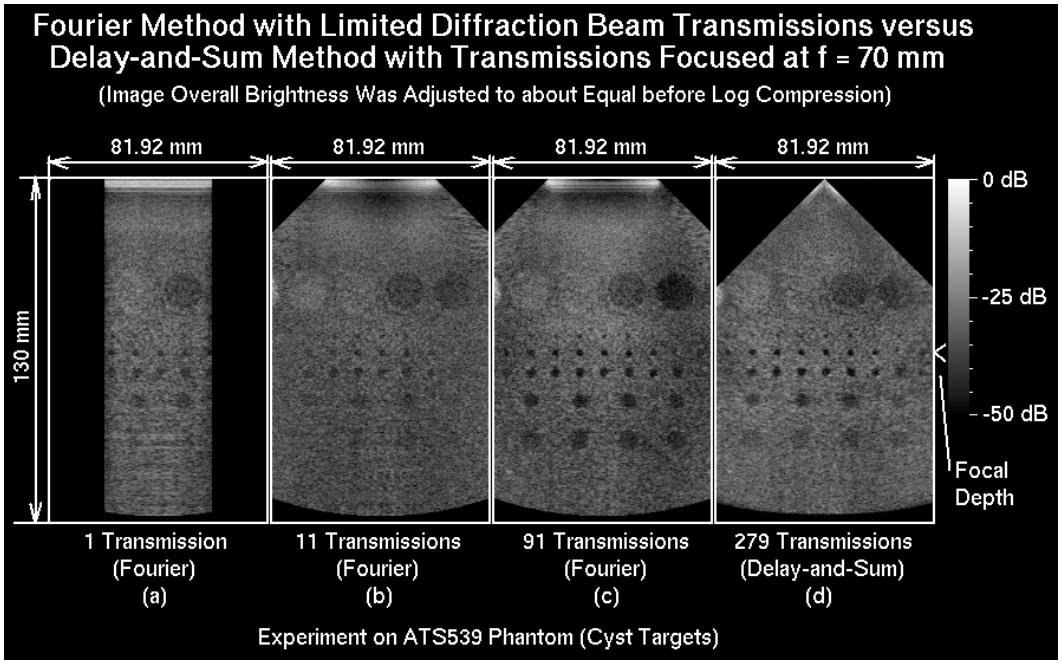

Fig. 11. The same as Fig. 9 except that the imaging area II of cystic objects of the ATS539 phantom (see Fig. 3) is used in the experiments.

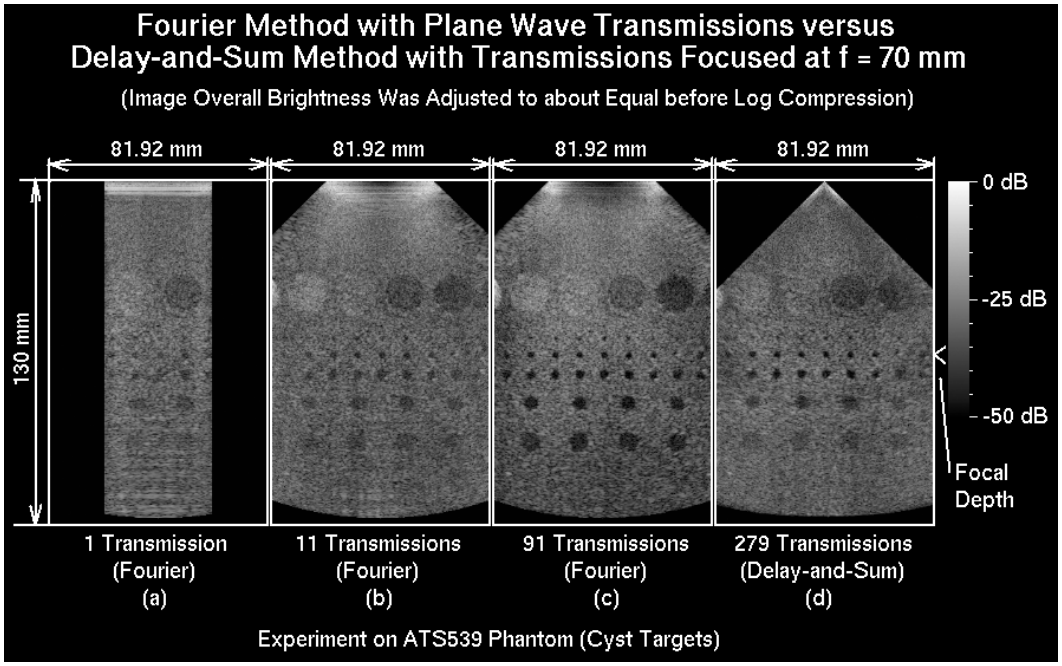

Fig. 12. The same as Fig. 11, except that steered plane waves are used in transmissions instead of limited-diffraction array beams.

structed images in spatial domain or its spectrum in spatial Fourier domain obtained from different transmissions, one obtains the final image. The superposition in spatial domain can be done either coherently (increase image resolution and contrast) or incoherently (reduce speckles) [59], [60]. However, in frequency domain, the superposition can be done only coherently, which in theory is equal to the superposition in the space domain. The superposition also will increase the field of view of the final image.

B. Sampling Constraints

The basic sampling constraint to implement (10) and (11) is to meet the Nyquist sampling rule [84] in both time and spatial domains so that signals can be recovered. In the echo Fourier domain, the sampling intervals in both x_1 and y_1 directions are determined by the transducer and must be smaller than a half of the minimum wavelength of the transducer to avoid aliasing or grating lobes. The sam-

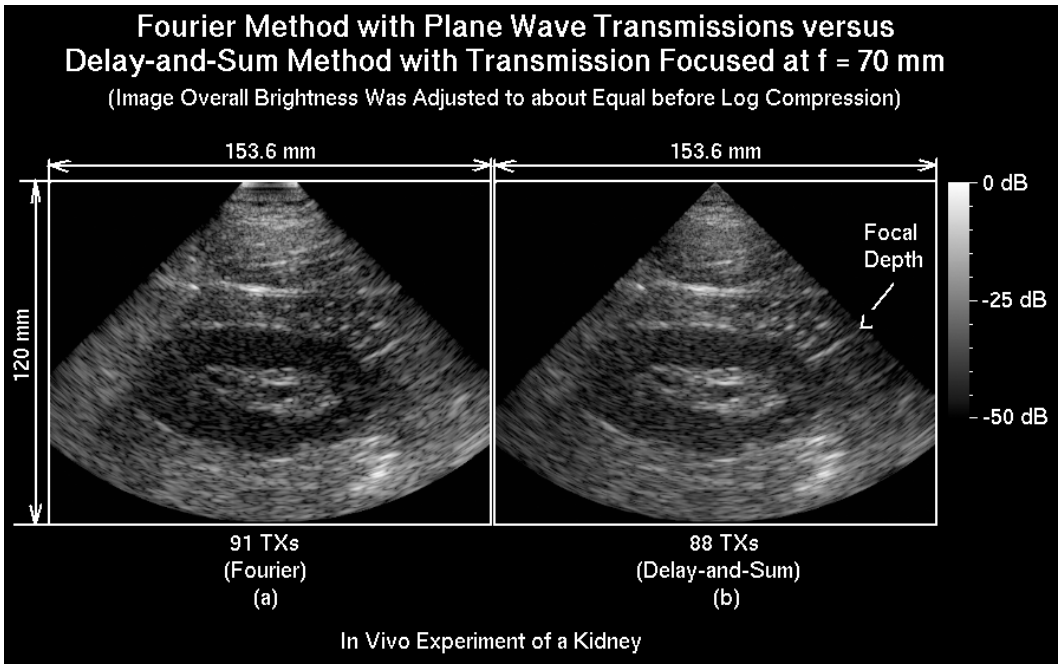

Fig. 13. *In vivo* experiments of a right kidney of a volunteer. An Acuson V2 probe of 128 element, 2.5-MHz center frequency, 19.2-mm aperture, 0.15-mm pitch, and 14-mm elevation with 68-mm elevation focal depth is used. The depth of images is 120 mm. Data are acquired at the highest frame rate that the HFR system is allowed for the depth (187 μs between transmissions or 5348 frames/second for a speed of sound of 1540 m/s). (a) Image reconstructed with 91 steered plane wave transmissions (59 frames/second). (b) Image reconstructed with the delay-and-sum method with a fixed focal depth of 70 mm and 88 transmissions (61 frames/second).

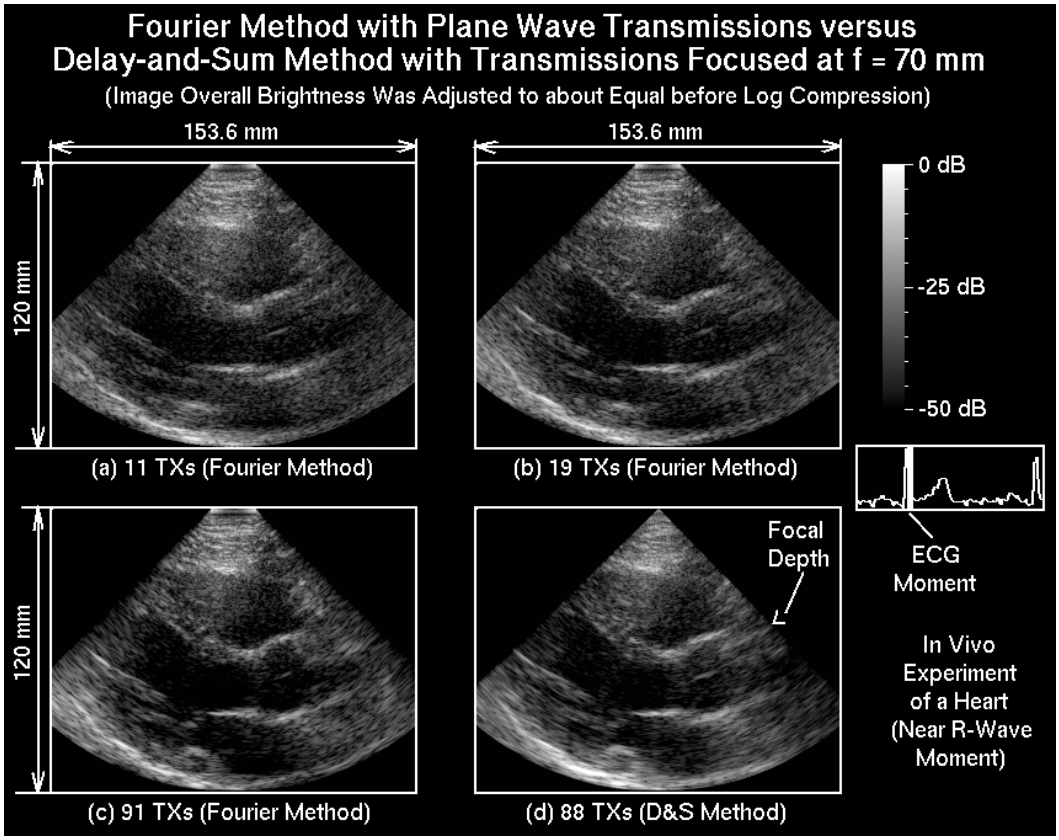

Fig. 14. *In vivo* experiments of the heart of a volunteer. The transducer parameters, the depth of images, and the settings of the HFR imaging system are the same as those in Fig. 13. Data acquisition of the heart is triggered and synchronized by an ECG signal to get images at the desired heart cycle moments (see the ECG display on the right-hand side panel). Image reconstructed with (a) 11 (486 frames/second), (b) 19 (281 frames/second), and (c) 91 (59 frames/second) steered plane wave transmissions. (d) Image reconstructed with the delay-and-sum method with a fixed focal depth of 70 mm and 88 transmissions (61 frames/second).

pling interval in time should be smaller than half of the smallest period of the signal frequency component. For limited-diffraction array beam transmissions, if the sampling interval (pitch) of the transducer is bigger than a half of the minimum wavelength, the image resolution will be lower, and the field of view may be limited because the maximum weighting wave number in transmission is limited. Another sampling interval to consider is in the spatial Fourier domain, (k'_x, k'_y, k'_z), of the object function. For a big object, the sampling interval must be small to get a large field of view and to avoid aliasing.

C. Under Sampled Aperture

To reduce effects of under-sampled aperture, which is the case for our 3.5 MHz transducer, one can apply a phase shift to compensate for the steered plane wave after echo signals are received [59], [60]. After the compensation, echoes would be effectively the same as if the array transducer were physically rotated in the transmission directions. This reduces aliasing caused by an under sampled aperture.

D. Windowing

Various windows could be applied to increase image reconstruction quality. For example, transducer aperture could be apodized to reduce sidelobes while sacrificing some image resolution and energy efficiency. Windows also could be added to the Fourier domain of the object function to reduce sidelobes, to the temporal frequency domain to remove unwanted frequency components, as well as to the spatial Fourier domain of echoes.

E. Finite Aperture and Image Resolution

The theory of the HFR imaging method was developed with the assumption that the transducer aperture is infinitely large. However, the aperture of a practical transducer is always finite. As is well-known from Goodman's book [84], a finite aperture will decrease image resolution. This is also clear from (16) in which any reduction in the size of the transducer aperture, $\sum_1$, will result in a convolution of the aperture function with the kernel (Green's function) in space in the Rayleigh-Sommerfeld diffraction formula, reducing image resolution.

F. Motion Artifacts

Because multiple frames of images may be used to form an image of a larger field of view with the extended HFR imaging theory, motion artifacts may be a concern as more and more frames of images are used. However, from the *in vivo* experiment of both kidney and heart with 91 transmissions, the artifacts are not noticeable (Fig. 12 shows the moment of the heart at the beginning of systole). This is because each subimage reconstructed with the HFR imaging method [27] does not have motion artifacts, and the number of transmissions is relatively small. In addition, because the transducer aperture is only 19.2 mm, at a larger distance, the number of subimages superposed at any given point is much smaller than 91. Motion artifacts of the extended HFR imaging method have been studied preliminarily [95]. Results show that this method is not sensitive to the motion, except when the number of transmissions is large (lower frame rate) and the depth is small. Further studies on motion artifacts, including motion of the heart during systole, will be carried out in the future.

VII. Conclusions

A HFR imaging theory was developed in 1997 [27], in which a pulsed plane wave was used in transmission, and limited-diffraction array beam weightings were applied to received echo signals to produce a spatial Fourier transform of object function for 3-D image reconstruction. In addition, the use of steered plane waves in transmissions to increase image field of view and reduce speckle noises [27], [28], [59], [60] or the use of limited-diffraction array beams [26], [29], [32] in transmission to increase field of view and spatial Fourier domain coverage to increase image resolution was suggested. In this paper, the HFR imaging theory was extended to include explicitly various transmission schemes such as multiple limited-diffraction array beams and steered plane waves [61], [62] (the first report was given in [61]). Moreover, limited-diffraction array beam weightings of received echo signals over a 2-D transducer aperture were proved to be the same as a 2-D Fourier transform of these signals over the same aperture [61], [62]. Because image frame rate is inversely proportional to the number of transmissions used to obtain a single frame of image, the extended theory provides a continuous compromise between image quality and frame rate. This is desirable in applications in which HFR imaging is not crucial, such as imaging of livers and kidneys, high quality images can be reconstructed at the expense of image frame rate.

Computer simulations, *in vitro* and *in vivo* experiments were performed to verify the extended theory. Both simulations and experiments (*in vitro* and *in vivo*) show that the extended theory can be used to reconstruct high quality images with little motion artifacts as compared to the conventional delay-and-sum method of a fixed transmission focus as well as the delay-and-sum method that synthesizes its dynamic transmission focuses with a montage process. Because the method can be implemented with the FFT that has very high computation efficiency, imaging systems that use the method would be simplified greatly. This is important for 3-D imaging with a fully populated 2-D array transducer in which the computation efficiency and image frame rate are of paramount importance. In addition, limited-diffraction array beam transmissions do not need time or phase delay to steer the beams that may allow a single or a small number of transmitters to replace over 10,000 independent transmitters in 3-D imaging, further simplifying the imaging systems [62].

The future work includes *in vivo* experiments with limited-diffraction array beam transmissions after the modifications of the firmware and software of the HFR imaging system, blood flow imaging, motion artifacts study, harmonic imaging, as well as hardware implementation of the extended theory.

Acknowledgment

The authors appreciate Mr. Jing Wang's help in the *in vivo* experiments and his help in reprocessing some of the figures.

References

[1] J. A. Stratton, *Electromagnetic Theory*. New York: McGraw-Hill, 1941, p. 356.
[2] J. Durnin, "Exact solutions for nondiffracting beams. I. The scalar theory," *J. Opt. Soc. Amer. A*, vol. 4, no. 4, pp. 651–654, 1987.
[3] J. Durnin, J. J. Miceli, Jr., and J. H. Eberly, "Diffraction-free beams," *Phys. Rev. Lett.*, vol. 58, pp. 1499–1501, Apr. 13, 1987.
[4] J.-y. Lu and J. F. Greenleaf, "Sidelobe reduction for limited diffraction pulse-echo systems," *IEEE Trans. Ultrason., Ferroelect., Freq. Contr.*, vol. 40, no. 6, pp. 735–746, Nov. 1993.
[5] G. Indebetow, "Nondiffracting optical fields: Some remarks on their analysis and synthesis," *J. Opt. Soc. Amer. A*, vol. 6, pp. 150–152, Jan. 1989.
[6] F. Gori, G. Guattari, and C. Padovani, "Model expansion for J0-correlated Schell-model sources," *Opt. Commun.*, vol. 64, pp. 311–316, Nov. 15, 1987.
[7] K. Uehara and H. Kikuchi, "Generation of near diffraction-free laser beams," *Appl. Phys. B*, vol. 48, pp. 125–129, 1989.
[8] L. Vicari, "Truncation of nondiffracting beams," *Opt. Commun.*, vol. 70, pp. 263–266, Mar. 15, 1989.
[9] M. Zahid and M. S. Zubairy, "Directionally of partially coherent Bessel-Gauss beams," *Opt. Commun.*, vol. 70, pp. 361–364, Apr. 1, 1989.
[10] J. Ojeda-Castaneda and A. Noyola-Iglesias, "Nondiffracting wavefields in grin and freespace," *Microwave Opt. Technol. Lett.*, vol. 3, pp. 430–433, Dec. 1990.
[11] D. K. Hsu, F. J. Margetan, and D. O. Thompson, "Bessel beam ultrasonic transducer: Fabrication method and experimental results," *Appl. Phys. Lett.*, vol. 55, no. 20, pp. 2066–2068, Nov. 13, 1989.
[12] P. D. Fox, J. Cheng, and J.-y. Lu, "Theory and experiment of Fourier-Bessel field calculation and tuning of a PW annular array," *J. Acoust. Soc. Amer.*, vol. 113, no. 5, pp. 2412–2423, May 2003.
[13] P. Fox, J. Cheng, and J.-y. Lu, "Fourier-Bessel field calculation and tuning of a CW annular array," *IEEE Trans. Ultrason., Ferroelect., Freq. Contr.*, vol. 49, pp. 1179–1190, Sep. 2002.
[14] H. Peng and J.-y. Lu, "High frame rate 2-D and 3-D imaging with a curved or cylindrical array," in *Proc. IEEE Ultrason. Symp.*, 2002, pp. 1725–1728.
[15] J.-y. Lu, J. Cheng, and B. Cameron, "Low sidelobe limited diffraction optical coherence tomography," in *Coherence Domain Optical Methods in Biomedical Science and Clinical Applications*. V. V. Tuchin, J. A. Izatt, and J. G. Fujimoto, Eds. *Proc. SPIE* vol. 4619, pp. 300–311, 2002.
[16] J.-y. Lu, J. Wang, H. Peng, and J. Cheng, "Increasing frame rate of limited diffraction imaging system with code excitations," in *Acoustical Imaging*. vol. 26, R. G. Maev, Ed. 2002, pp. 467–475.
[17] J.-y. Lu, J. Cheng, and H. Peng, "Sidelobe reduction of images with coded limited diffraction beams," in *Proc. IEEE Ultrason. Symp.*, 2001, pp. 1565–1568.
[18] J.-y. Lu, "A study of signal-to-noise ratio of the Fourier method for construction of high frame rate images," in *Acoustical Imaging*. vol. 24, H. Lee and G. Wade, Eds. 2000, pp. 401–406.
[19] J.-y. Lu and A. Liu, "An X wave transform," *IEEE Trans. Ultrason., Ferroelect., Freq. Contr.*, vol. 47, pp. 1472–1481, Nov. 2000.
[20] S. He and J.-y. Lu, "Sidelobe reduction of limited diffraction beams with Chebyshev aperture apodization," *J. Acoust. Soc. Amer.*, vol. 107, pp. 3556–3559, June 2000.
[21] D. Ding and J.-y. Lu, "Second harmonic generation of the nth-order Bessel beams," *Phys. Rev. E*, vol. 61, pp. 2038–2041, Feb. 2000.
[22] D. Ding and J.-y. Lu, "Higher-order harmonics of limited diffraction Bessel beams," *J. Acoust. Soc. Amer.*, vol. 107, pp. 1212–1214, Mar. 2000.
[23] J.-y. Lu and S. He, "Effects of phase aberration on high frame rate imaging," *Ultrasound Med. Biol.*, vol. 26, no. 1, pp. 143–152, 2000.
[24] J.-y. Lu and S. He, "High frame rate imaging with a small number of array elements," *IEEE Trans. Ultrason., Ferroelect., Freq. Contr.*, vol. 46, pp. 1416–1421, Nov. 1999.
[25] J.-y. Lu and S. He, "Optical X waves communications," *Opt. Communi.*, vol. 161, pp. 187–192, Mar. 15 1999.
[26] J.-y. Lu, "Transmit-receive dynamic focusing with limited diffraction beams," in *Proc. IEEE Ultrason. Symp.*, 1997, pp. 1543–1546.
[27] J.-y. Lu, "2-D and 3-D high frame rate imaging with limited diffraction beams," *IEEE Trans. Ultrason., Ferroelect., Freq. Contr.*, vol. 44, pp. 839–856, July 1997.
[28] J.-y. Lu, "Experimental study of high frame rate imaging with limited diffraction beams," *IEEE Trans. Ultrason., Ferroelect., Freq. Contr.*, vol. 45, pp. 84–97, Jan. 1998.
[29] J.-y. Lu, "Improving accuracy of transverse velocity measurement with a new limited diffraction beam," in *Proc. IEEE Ultrason. Symp.*, 1996, pp. 1255–1260.
[30] J.-y. Lu, "Designing limited diffraction beams," *IEEE Trans. Ultrason., Ferroelect., Freq. Contr.*, vol. 44, pp. 181–193, Jan. 1997.
[31] J.-y. Lu, M. Fatemi, and J. F. Greenleaf, "Pulse-echo imaging with X wave," in *Acoustical Imaging*. vol. 22, P. Tortoli, Ed. 1996, pp. 191–196.
[32] J.-y. Lu, "Limited diffraction array beams," *Int. J. Imaging Syst. Technol.*, vol. 8, pp. 126–136, Jan. 1997.
[33] J.-y. Lu, "Producing bowtie limited diffraction beams with synthetic array experiment," *IEEE Trans. Ultrason., Ferroelect., Freq. Contr.*, vol. 43, pp. 893–900, Sep. 1996.
[34] J.-y. Lu, "Bowtie limited diffraction beams for low-sidelobe and large depth of field imaging," *IEEE Trans. Ultrason., Ferroelect., Freq. Contr.*, vol. 42, pp. 1050–1063, Nov. 1995.
[35] J.-y. Lu, H. Zou, and J. F. Greenleaf, "A new approach to obtain limited diffraction beams," *IEEE Trans. Ultrason., Ferroelect., Freq. Contr.*, vol. 42, pp. 850–853, Sep. 1995.
[36] J.-y. Lu and J. F. Greenleaf, "Comparison of sidelobes of limited diffraction beams and localized waves," in *Acoustical Imaging*. vol. 21, J. P. Jones, Ed. 1995, pp. 145–152.
[37] J.-y. Lu, X.-L. Xu, H. Zou, and J. F. Greenleaf, "Application of Bessel beam for Doppler velocity estimation," *IEEE Trans. Ultrason., Ferroelect., Freq. Contr.*, vol. 42, pp. 649–662, July 1995.
[38] J.-y. Lu and J. F. Greenleaf, "A study of two-dimensional array transducers for limited diffraction beams," *IEEE Trans. Ultrason., Ferroelect., Freq. Contr.*, vol. 41, pp. 724–739, Sep. 1994.
[39] J.-y. Lu, H. Zou, and J. F. Greenleaf, "Biomedical ultrasound beam forming," *Ultrasound Med. Biol.*, vol. 20, pp. 403–428, July 1994.
[40] J.-y. Lu, T. K. Song, R. R. Kinnick, and J. F. Greenleaf, "In vitro and in vivo real-time imaging with ultrasonic limited diffraction beams," *IEEE Trans. Med. Imag.*, vol. 12, pp. 819–829, Dec. 1993.
[41] J.-y. Lu and J. F. Greenleaf, "Producing deep depth of field and depth-independent resolution in NDE with limited diffraction beams," *Ultrason. Imag.*, vol. 15, pp. 134–149, Apr. 1993.
[42] T. K. Song, J.-y. Lu, and J. F. Greenleaf, "Modified X waves with improved field properties," *Ultrason. Imag.*, vol. 15, pp. 36–47, Jan. 1993.
[43] J.-y. Lu and J. F. Greenleaf, "Diffraction-limited beams and their applications for ultrasonic imaging and tissue characterization," in *New Developments in Ultrasonic Transducers and Transducer Systems*. F. L. Lizzi, Ed. *Proceedings of SPIE* vol. 1733, pp. 92–119, 1992.
[44] J.-y. Lu and J. F. Greenleaf, "Nondiffracting X waves—Exact solutions to free-space scalar wave equation and their finite

aperture realizations," *IEEE Trans. Ultrason., Ferroelect., Freq. Contr.*, vol. 39, pp. 19–31, Jan. 1992.

[45] J.-y. Lu and J. F. Greenleaf, "Experimental verification of nondiffracting X waves," *IEEE Trans. Ultrason., Ferroelect., Freq. Contr.*, vol. 39, pp. 441–446, May 1992.

[46] J.-y. Lu and J. F. Greenleaf, "Evaluation of a nondiffracting transducer for tissue characterization," in *Proc. IEEE Ultrason. Symp.*, 1990, pp. 795–798.

[47] J.-y. Lu and J. F. Greenleaf, "Pulse-echo imaging using a nondiffracting beam transducer," *Ultrasound Med. Biol.*, vol. 17, pp. 265–281, May 1991.

[48] J.-y. Lu and J. F. Greenleaf, "Ultrasonic nondiffracting transducer for medical imaging," *IEEE Trans. Ultrason., Ferroelect., Freq. Contr.*, vol. 37, pp. 438–447, Sep. 1990.

[49] M. A. Porras, A. Parola, D. Faccio, A. Dubietis, and P. Di Trapani, "Nonlinear unbalanced Bessel beams: Stationary conical waves supported by nonlinear losses," *Phys. Rev. Lett.*, vol. 93, 153902, 2004.

[50] M. Kolesik, E. M. Wright, and J. V. Moloney, "Dynamic nonlinear X waves for femtosecond pulse propagation in water," *Phys. Rev. Lett.*, vol. 92, 253901, 2004.

[51] C. Conti and S. Trillo, "Nonspreading wave packets in three dimensions formed by an ultracold Bose gas in an optical lattice," *Phys. Rev. Lett.*, vol. 92, 120404, 2004.

[52] P. Di Trapani, G. Valiulis, A. Piskarskas, O. Jedrkiewicz, J. Trull, C. Conti, and S. Trillo, "Spontaneously generated x-shaped light bullets," *Phys. Rev. Lett.*, vol. 91, 093904, 2003.

[53] C. Conti, S. Trillo, P. Di Trapani, G. Valiulis, A. Piskarskas, O. Jedrkiewicz, and J. Trull, "Nonlinear electromagnetic X waves," *Phys. Rev. Lett.*, vol. 90, 170406, 2003.

[54] J. Salo, J. Fagerholm, A. T. Friberg, and M. M. Salomaa, "Nondiffracting bulk-acoustic X waves in crystals," *Phys. Rev. Lett.*, vol. 83, pp. 1171–1174, 1999.

[55] P. Saari and K. Reivelt, "Evidence of X-shaped propagation-invariant localized light waves," *Phys. Rev. Lett.*, vol. 79, pp. 4135–4138, 1997.

[56] T. Wulle and S. Herminghaus, "Nonlinear optics of Bessel beams," *Phys. Rev. Lett.*, vol. 70, pp. 1401–1404, 1993.

[57] C. Day, "Intense X-shaped pulses of light propagate without spreading in water and other dispersive media," *Phys. Today*, vol. 57, pp. 25–26, Oct. 2004.

[58] G. Wade, "Human uses of ultrasound: Ancient and modern," *Ultrasonics*, vol. 38, pp. 1–5, 2000.

[59] J.-y. Lu, "Nonlinear processing for high frame rate imaging," *J. Ultrasound Med.*, vol. 18, (Suppl.) p. S50, Mar. 1999.

[60] J.-y. Lu and S. He, "Increasing field of view of high frame rate ultrasonic imaging," *J. Acoust. Soc. Amer.*, vol. 107, pt. 2, p. 2779, May 2000.

[61] J. Cheng and J.-y. Lu, "Fourier based imaging method with steered plane waves and limited-diffraction array beams," in *Proc. IEEE Ultrason. Symp.*, 2005, pp. 1976–1979.

[62] J.-y. Lu, J. Cheng, and J. Wang, "High frame rate imaging system for limited diffraction array beam imaging with square-wave aperture weightings," *IEEE Trans. Ultrason., Ferroelect., Freq. Contr.*, submitted for publication.

[63] S. J. Nortan and M. Linzer, "Ultrasonic reflectivity imaging in three dimensions: Exact inverse scattering solution for plane, cylindrical and spherical aperture," *IEEE Trans. Biomed. Eng.*, vol. BME-28, pp. 202–220, Feb. 1981.

[64] K. Nagai, "Fourier domain reconstruction of ultrasonic 2-D and 3-D images using exact inverse scattering solution," in *Proc. IEEE Ultrason. Symp.*, 1985, pp. 804–807.

[65] K. Nagai, "A new synthetic-aperture focusing method for ultrasonic B-scan imaging by the Fourier transform," *IEEE Trans. Ultrason., Ferroelect., Freq. Contr.*, vol. SU-32, no. 4, pp. 531–536, July 1985.

[66] M. Soumekh, "Depth-focused interior echo imaging," *IEEE Trans. Image Processing*, vol. 8, pp. 1608–1618, Nov. 1999.

[67] M. Soumekh, "Array imaging with beam-steered data," *IEEE Trans. Image Processing*, vol. 1, pp. 379–390, July 1992.

[68] J. T. Ylitalo and H. Ermert, "Ultrasound synthetic aperture imaging: Monostatic approach," *IEEE Trans. Ultrason., Ferroelect., Freq. Contr.*, vol. 41, pp. 333–339, May 1994.

[69] J. T. Ylitalo, "Synthetic aperture ultrasound imaging using a convex array," in *Proc. IEEE Ultrason. Symp.*, 1995, pp. 1337–1340.

[70] L. J. Busse, "Three-dimensional imaging using a frequency domain synthetic aperture focusing technique," *IEEE Trans. Ultrason., Ferroelect., Freq. Contr.*, vol. 39, pp. 174–179, Mar. 1992.

[71] T. Rastello, C. Hass, D. Vray, M. Krueger, K. Schroeder, E. Brusseau, G. Gimenez, and H. Ermert, "A new Fourier-based multistatic synthetic aperture focusing technique for intravascular ultrasound imaging," in *Proc. IEEE Ultrason. Symp.*, 1998, pp. 1725–1728.

[72] M. A. Haun, D. L. Jones, and W. D. O'Brien, "Efficient three-dimensional imaging from a small cylindrical aperture," *IEEE Trans. Ultrason., Ferroelect., Freq. Contr.*, vol. 49, pp. 861–870, July 2002.

[73] M. A. Moehring, F. E. Barber, and J. R. Klepper, "Quasi real-time Fourier reconstructive imaging from acoustic backscatter data," in *Proc. IEEE Ultrason. Symp.*, 1990, pp. 1485–1490.

[74] Z. M. Benenson, A. B. Elizarov, T. V. Yakovleva, and W. D. O'Brien, "Approach to 3-D ultrasound high resolution imaging for mechanically moving large-aperture transducer based upon Fourier transform," *IEEE Trans. Ultrason., Ferroelect., Freq. Contr.*, vol. 49, pp. 1665–1685, Dec. 2002.

[75] M. K. Jeong, S. J. Kwon, T. K. Song, and M. H. Bae, "Realization of sinc waves in ultrasound imaging systems," *Ultrason. Imag.*, vol. 21, pp. 173–185, July 1999.

[76] M. K. Jeong, T. K. Song, S. B. Park, and J. B. Ra, "Generation of sinc wave by one-dimensional array for applications in ultrasonic imaging," *IEEE Trans. Ultrason., Ferroelect., Freq. Contr.*, vol. 43, pp. 285–295, Mar. 1996.

[77] J.-y. Lu and J. L. Waugaman, "Development of a linear power amplifier for high frame rate imaging system," in *Proc. IEEE Ultrason. Symp.*, 2004, pp. 1413–1416.

[78] J.-y. Lu, "A multimedia example," *IEEE Trans. Ultrason., Ferroelect., Freq. Contr.*, vol. 50, p. 1078, Sep. 2003.

[79] C. S. Kino, *Acoustic Waves: Devices, Imaging and Analog Signal Processing*. Englewood Cliffs, NJ: Prentice-Hall, 1987.

[80] R. Bracewell, *The Fourier Transform and Its Applications*. New York: McGraw-Hill, 1965.

[81] A. C. Kak and M. Slaney, *Principle of Computerized Tomographic Imaging*. New York: IEEE Press, 1987.

[82] M. Born and E. Wolf, *Principles of Optics*. 7th ed. Cambridge: Cambridge Univ. Press, 1999.

[83] G. C. Sherman, "Application of the convolution theorem to Rayleigh's integral formulas," *J. Opt. Soc. Amer.*, vol. 57, pp. 546–547, Apr. 1967.

[84] J. W. Goodman, *Introduction to Fourier Optics*. New York: McGraw-Hill, 1968.

[85] J. Shen, H. Wang, C. Cain, and E. S. Ebbini, "A post beamforming processing technique for enhancing conventional pulse-echo ultrasound imaging contrast resolution," in *Proc. IEEE Ultrason. Symp.*, 1995, pp. 1319–1322.

[86] C. B. Burckhardt, H. Hoffmann, and P. A. Grandchamp, "Ultrasound Axicon: A device for focusing over a large depth," *J. Acoust. Soc. Amer.*, vol. 54, pp. 1628–1630, Dec. 1973.

[87] F. S. Foster, M. S. Patterson, M. Arditi, and J. W. Hunt, "The conical scanner: A two transducer ultrasound scatter imaging technique," *Ultrason. Imag.*, vol. 3, pp. 62–82, Apr. 1981.

[88] D.-L. D. Liu, "Plane wave scanning reception and receiver," U.S. Patent, No. 6685641 B2, issued Feb. 3, 2004.

[89] G. E. Tupholme, "Generation of acoustic pulses by baffled plane pistons," *Mathematika*, vol. 16, pp. 209–224, 1969.

[90] P. R. Stepanishen, "The time-dependent force and radiation impedance on a piston in a rigid infinite planar baffle," *J. Acoust. Soc. Amer.*, vol. 49, no. 3, pp. 841–849, 1971.

[91] G. R. Harris, "Review of transient field theory for a baffled planar piston," *J. Acoust. Soc. Amer.*, vol. 70, pp. 1–20, 1981.

[92] J. A. Jensen and N. B. Svendsen, "Calculation of pressure fields from arbitrarily shaped, apodized, and excited ultrasound transducers," *IEEE Trans. Ultrason., Ferroelect., Freq. Contr.*, vol. 39, no. 2, pp. 262–267, Mar. 1992.

[93] J. A. Jensen, "A new calculation procedure for spatial impulse responses in ultrasound," *J. Acoust. Soc. Amer.*, vol. 105, no. 6, pp. 3266–3274, 1999.

[94] J. Lubbers and R. Graaff, "A simple and accurate formula for the sound velocity in water," *Ultrasound Med. Biol.*, vol. 24, no. 7, pp. 1065–1068, 1998.

[95] J. Wang and J.-y. Lu, "A study of motion artifacts of Fourier-based image construction," in *Proc. IEEE Ultrason. Symp.*, 2005, pp. 1439–1442.

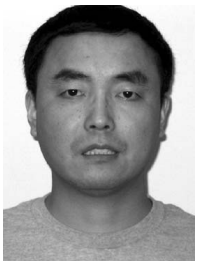

Jiqi Cheng was born in Jiangsu, China, in 1975. He received the B.S. degree and the M.S. degree in biomedical engineering in 1998 and 2000, respectively, both from Southeast University, Nanjing, China. He is currently pursing his doctorate degree in the Department of Bioengineering at the University of Toledo, OH.

His research interests in ultrasound include field calculation, beam forming, transducer modeling, image formation, and medical imaging.

Jian-yu Lu (S'86–M'88–SM'99) received the B.S. degree in electrical engineering in February 1982 from Fudan University, Shanghai, China; the M.S. degree in acoustics in 1985 from Tongji University, Shanghai, China; and the Ph.D. degree in biomedical engineering in 1988 from Southeast University, Nanjing, China.

From 1997 to the present, Dr. Lu has been a professor in the Department of Bioengineering at the University of Toledo, Toledo, OH, and an adjunct professor of medicine at the Medical University of Ohio, Toledo, OH. He served as a Graduate Director of the Department of Bioengineering at the University of Toledo from 1999–2002. Before joining the University of Toledo, he was an associate professor of biophysics at the Mayo Medical School and an associate consultant at the Department of Physiology and Biophysics, Mayo Clinic/Foundation, Rochester, MN. His research interests are in acoustic imaging and tissue identification, medical ultrasonic transducers, and ultrasonic beam forming and propagation.

Dr. Lu has received the Outstanding Paper Award from the UFFC society for two of his papers published in the *IEEE Transactions on Ultrasonics, Ferroelectrics, and Frequency Control* (UFFC) in 1992 for the discovery of X waves that, in theory, can propagate to an infinite distance without spreading (diffraction-free). These waves have potential applications in medical imaging (in both ultrasound and optics). Dr. Lu received the Edward C. Kendall (a Nobel Laureate at Mayo Clinic) Award from the Mayo Alumni Association, Mayo Foundation, in 1992, for his meritorious research; the FIRST Award from the National Institutes of Health (NIH) in 1991; and the Biomedical Engineering Research Grant Award from the Whitaker Foundation in 1991, in addition to other long-term R01 type of NIH grant award.

Dr. Lu has been the Editor-in-Chief of the *IEEE Transactions on Ultrasonics, Ferroelectrics, and Frequency Control* since January 2002. He is a General Co-Chair of the 2008 IEEE International Ultrasonics Symposium (IEEE IUS) that will be held in Beijing, China. In addition, he served as the Technical Program Chair of the 2001 IEEE IUS—a joint meeting with the World Congress on Ultrasonics (WCU) held in Atlanta, GA, in October 2001. He is a member of Group I (Medical Ultrasonics) of the Technical Program Committee of the IEEE IUS (since 2000). He also serves in both the UFFC Ultrasonics Committee and the UFFC Web Committee. He was an Exhibition Chair of the IEEE IUS for many years. Dr. Lu is a Fellow of the American Institute of Ultrasound in Medicine (AIUM) and a Senior Member of the IEEE UFFC Society, in addition to a Member of other professional societies such as the Acoustical Society of America (ASA), American Association for the Advancement of Science (AAAS), and Sigma Xi.